Marine Geology
January 2023, Volume 455, Pages 106968 (14p.)
https://doi.org/10.1016/j.margeo.2022.106968
https://archimer.ifremer.fr/doc/00811/92291/

Late Cretaceous evolution of chemical weathering at the northeastern South American margin inferred from mineralogy and Hf-Nd isotopes

Corentin Pauline [1, *], Pucéat Emmanuelle [1], Pellenard Pierre [1], Guiraud Michel [1], Blondet Justine [1], Bayon Germain [2], Adatte Thierry [3]

[1] Biogéosciences, UMR 6282 CNRS, Université Bourgogne Franche-Comté, 21000 Dijon, France
[2] Univ Brest, CNRS, Ifremer, Geo-Ocean, F-29280 Plouzané, France
[3] Institute of Earth Sciences, Géopolis, University of Lausanne, Lausanne, Switzerland

* Corresponding author : Pauline Corentin, email address : pauline.corentin21@gmail.com

Abstract :

The origin of the global temperature decrease that initiated the last greenhouse-icehouse transition about 90 million years ago still remains debated. Among the potential processes driving long-term climate evolution over million-year timescales, this study investigates the possible impact of the uplift-weathering connection on the late Cretaceous atmospheric CO2 drawdown and associated cooling.

We analysed a marine sediment record from the Demerara margin, using Nd and Hf isotopes in clay-size detrital fractions (ΔεHf(t)clay) together with bulk and clay mineralogy and major element abundances to reconstruct the evolution of tectonic uplift and chemical weathering intensity in northeastern South America during the late Cretaceous. Our data indicate that silicate weathering intensified on the northeastern South American margin during the middle Campanian and the Maastrichtian, concomitant with an uplift phase of the Guiana craton. We propose that the tectonic pulse highlighted by apatite fission track data, argon/argon dating and primary silicate mineral evolution, was accompanied by an accelerated chemical weathering, which presumably acted as a sink for atmospheric CO2. By contrast, during the earlier late Turonian to early Campanian, period of relative tectonic quiescence, climate most likely acted as the main driver controlling the evolution of chemical weathering intensity. The main phase of enhanced weathering induced by the uplift of the northeastern South American margin occurred during the Campanian, thereby postdating the onset of global seawater temperature decrease (late Turonian). By inference, this regional event is unlikely to have triggered late Cretaceous cooling but it may have acted as an additional factor stabilizing colder climate conditions at that time.

Highlights

► Use of paired Hf-Nd isotopes to constrain continental weathering in deep-time. ► Enhanced silicate weathering concomitant with an uplift phase of the Guiana craton. ► Tectonic uplift contributed to the late Cretaceous cooling. ► During relative tectonic quiescence, climate seems to control the evolution of chemical weathering intensity. ► Accelerating chemical weathering acted as an additional factor stabilizing colder climate conditions.

Keywords : Continental weathering, Isotopic geochemistry, Clay mineralogy, Palaeoclimate, Cretaceous

1. Introduction

The late Cretaceous was a period marked by major tectonic and climatic changes. While a global decrease of seawater temperature from the Turonian to the Maastrichtian is recorded by Tex_{86} and foraminiferal $\delta^{18}O$ proxy data at all latitudes, its origin remains unclear (Friedrich *et al.*, 2012 ; O'Brien *et al.*, 2017). A pronounced decrease in atmospheric CO_2 levels (pCO_2) at that time (Wang *et al.*, 2014) indicates that the late Cretaceous climate cooling was closely related to the global long-term carbon cycle. The same period was also characterized by major tectonic events such as the uplift of the West African and eastern South American margins (Harmann *et al.*, 1998 ; Gallagher & Brown, 1999 ; Jaspen *et al.*, 2012 ; Engelmann de Oliveira *et al.*, 2016 ; Green *et al.*, 2017, 2018 ; Mourlot *et al.*, 2018 ; Roddaz *et al.*, 2021), which could have impacted the carbon cycle through enhanced mechanical erosion and chemical weathering.

Indeed, among the processes driving the long-term carbon cycle, chemical weathering of silicate rocks on continents acts as a major sink of atmospheric CO_2 over million-year timescales. Chemical weathering depends on climatic parameters such as temperature and precipitation (White & Blum, 1995), but also on mechanical erosion rates. Continuous exposure of fresh rock surfaces by mechanical erosion promotes chemical weathering (Raymo & Ruddiman, 1988 ; West *et al.*, 2005 ; Gabet & Mudd, 2009), up to a threshold where, at

high denudation rates, detrital material is exported too rapidly to further sustain silicate weathering in soils (West *et al*., 2005 ; Gabet & Mudd, 2009). In active tectonic settings, such kinetically-limited weathering regimes typically lead to near-constant chemical weathering rates with increasing denudation rates (White & Blum, 1995 ; Gabet & Mudd, 2009 ; West, 2012). Therefore, the relationship between tectonic uplift and silicate weathering, and thus the net impact of this process on atmospheric carbon concentrations, is not straightforward and still needs to be explored. The major uplift phase of South Atlantic margins during the late Cretaceous major climate change could provide new insights to explore the interplay between climate and tectonic uplift.

In this study, we investigated a marine sediment record from Demerara Rise (ODP Site 1259) to explore the response of silicate weathering to the uplift of the northeastern margin of the South American continent, which occurred during the late Cretaceous from Guiana to Brazil (McConnell, 1968 ; Harman, 1998 ; Morais Neto *et al.*, 2009 ; Jaspen *et al.*, 2012 ; Green *et al.*, 2018). A multi-proxy approach based on Hf-Nd isotope analyses of clay-size detrital fractions combined with complementary geochemical and mineralogical data can provide unique insights into the evolution of continental chemical weathering through time (Bayon *et al.*, 2016 ; Corentin *et al.*, 2022; Bayon *et al*., 2022). Recently, the same approach has been successfully used to reconstruct the late Cretaceous evolution of silicate weathering along the southeastern Brazilian margin (Corentin *et al.*, 2022), showing that the formation of high topographic relief under arid climate conditions favoured mechanical erosion until the elevation was high enough to support high orographic precipitations and, consequently, enhanced silicate chemical weathering (Corentin *et al.*, 2022).

2. Setting

ODP Site 1259 (2354 meter depth) from Demerara Rise (Fig. 1) exhibits upper Cretaceous sediments from the Cenomanian to the Maastrichtian (Erbacher *et al.*, 2004). The samples were collected from two lithostratigraphic units (between 440 and 540 mbsf; Fig. 2, 3) : 1) a Turonian to Santonian interval composed of laminated calcareous claystone with organic matter, clayey chalk and limestone; and 2) a Campanian to late Maastrichtian interval, composed of nannofossil-rich clayey chalk, calcareous siltstone and glauconitic claystone (Fig. 2, 3 ; Supplementary Table 1 ; Erbacher *et al.*, 2004). These sediments were deposited in a marine setting evolving from shelf environments during the Cenomanian to upper bathyal environments in the early Campanian (Erbacher *et al.* 2005), under direct influence of terrigenous fluxes from the adjacent continental margin (März *et al.*, 2009).

The Demerara Rise, surrounded by the Guiana/Suriname (GS) and the Foz do Amazonas (FOZ) basins, is located on the northeastern South American margin (Fig. 1.A, 1.B), near the Guiana, Suriname and French Guiana coastal regions (Fig. 1.B). During the end of the early Cretaceous, a plate kinematic reorganization (~ 105 Ma), followed by a late Cenomanian-Turonian deformation led to the uplift of the Demerara plateau (Yang and Escalona, 2011; Basile *et al.*, 2013; Loncke *et al.*, 2020). The plateau became a structural high separating the Guiana/Suriname Basin and the Foz do Amazonas Basin and resulting in the isolation the Demerara plateau (Fig. 1.B; Loncke *et al.*, 2020). After the late Albian unconformity, the Demerara plateau evolved into a passive margin with a transition from shallow to deep marine conditions (Loncke *et al.*, 2020).

The Guiana Shield represents the main continental landmass that provides detrital sediment inputs to the Demerara Rise (Roddaz *et al.*, 2021 ; Fig. 1.B). During the late Cretaceous, this area corresponded to a low-elevation passive margin located in a humid equatorial climatic belt (Hay *et al.*, 2012 ; Sapin *et al.*, 2016).

3. Material and methods

A total of 88 samples from Site 1259 were analysed, spanning a period from the late Turonian to late Maastrichtian. The age model is based on the biostratigraphy published in Erbacher *et al.* (2004) and Gradstein *et al.* (2012).

3.1. Mineralogical analyses

Bulk sediment and clay (< 2 μm) mineralogical analyses were performed at the Biogeosciences Laboratory (University of Burgundy, France) using X-ray diffraction (XRD) with a Bruker Endeavor D4 diffractometer equipped with a Lynxeye detector, CuKα radiations and Ni filter, under 40 kV voltage and 25 mA intensity. The isolated clay fraction was analysed using the three treatments recommended by Moore and Reynolds (1997). Identification and semi-quantification of the mineral phases were performed with the software MacDiff 4.2.5 (Petschick, 2001) using the position of main diffraction peaks and the area of their main diffraction peaks, respectively. For clay mineralogy, the proportions were estimated after ethylene glycol solvated preparation using the main diffraction (d_{001}) peak.

The (Illite+Chlorite)/smectite ((I+C)/S), (Opal+Clinoptilolite)/Calcite ((O+C)/Ca) and Feldspar/Clays (Feld./Clays) ratios were calculated using the mean peak area of each mineral. The uncertainty of the relative proportions of clay minerals is estimated as < 5%, based on replicate analyses of samples and the internal procedure of quantification using MacDiff on mixtures of clay minerals in known proportions.

The clay fractions of 3 samples were dispersed in distilled water and butylamine solution, and deposited on a carbon formvar Cu grid for Transmission Electron Microscopy (TEM) observations. Images of clay particles were performed using a MET Hitachi 4800 at the INRAE of the University of Burgundy (France).

3.2. Geochemical analyses

Major element abundances and CIA

X-ray fluorescence spectroscopy (XRF) was used to determine whole-rock major element abundances (SiO_2, TiO_2, Al_2O_3, Fe_2O_3, MnO, MgO, CaO, Na_2O, K_2O and P_2O_5; Supplementary Table 1) at the University of Lausanne, using a wavelength-dispersive PANalytical AxiosmAX spectrometer fitted with a 4 kW Rh X-ray tube. Fused disks were prepared from 1.2 g of calcined sample powder mixed with lithium tetraborate (1:5 mixture) for the analyses. A number of 21 international silicate rock reference materials was used for the calibration. The data are reported on a loss of ignition (LOI)-free basis (Supplementary Table 1). The limits of detection are in the range 20 to 80 ppm for major elements depending on the element concerned.

The chemical index of alteration (CIA) was calculated and used as a proxy of chemical weathering intensity (Nesbitt & Young, 1982). Because our samples of bulk sediments display relatively high carbonate contents (between 14-91 %), detrital CaO contents were estimated using the method of McLennan (1993), which consists of replacing CaO* by Na_2O in the following calculation: [Al_2O_3/(Al_2O_3 + Na_2O + CaO* + K_20] x 100 (where CaO* represents the amount of CaO in the silicate fraction of the sediments). The CIA is generally interpreted as the extent to which feldspar, which contains relatively mobile Ca, Na and K, has been weathered and converted to Al-rich clay minerals (Nesbitt & Young, 1982).

Hf, Zr and REE concentrations and Hf-Nd isotopes

Following the protocol described in Bayon *et al.* (2002) and modified in Corentin *et al.* (2022), a total of 23 samples (8 samples collected in claystone lithology and 15 samples collected in chalk lithology ; Supplementary Table 1) were selected for geochemical analyses. This protocol includes a sequential leaching procedure that successively removes carbonates, Fe-Mn oxyhydroxides and organic matter. Then, the clay-size detrital fraction (< 2µm) is separated from the residual sediments by decantation and submitted to a second leaching

procedure. Following clay extraction, about 65 mg of dry powdered samples were digested by alkaline fusion after addition of a Tm spike (Barrat *et al.*, 1996).

Finally, ion exchange chromatography was used to isolate purified Nd and Hf fractions using columns packed with AG-50W-X8 and Ln-Spec resin for Nd and AG1-X8 and Ln-Spec for Hf, following the protocols described in Chu *et al.* (2002) and Bayon *et al.* (2012), respectively.

Concentrations of REE, Hf and Zr were measured by inductively coupled plasma mass spectrometry (ICP-MS) on a Thermo Scientific X-Series II at the Pôle Spectrométrie Océan (Brest, France). Details about measured elemental masses, polyatomic interference corrections and the quantification method are given in Barrat *et al.* (1996) and Bayon *et al.* (2009b). External reproducibility and accuracy were estimated by replicate analyses of four certified reference materials from the United States Geological Survey (BCR-2, BIR-1, MAG-1, BHVO-2 ; Supplementary Table 2). Analytical reproducibility was better than 2% for all elements. Deviations from the reference values for BHVO-2, BCR-2 and BIR-1 (Jochum *et al.*, 2016) were always < 10% RSD.

Hafnium and neodymium isotope compositions of studied samples were measured on a MC-ICP-MS Neptune Plus (Thermo Scientific) at the ENS of Lyon (France) with a sample-standard bracketing method, using concentration-matched solutions of JMC475 and JNdi-1 standards, respectively. The instrumental mass bias were corrected applying an exponential law, using $^{146}Nd/^{144}Nd = 0.7219$ and $^{179}Hf/^{177}Hf = 0.7325$. Nd and Hf procedural blanks were respectively better than 6 pg and 10 pg.

The analytical session gave a $^{176}Hf/^{177}Hf$ ratio of 0.282163 ± 0.000008 (2 s.d., n=21) corresponding to an external reproducibility of ± 0.28ε (2 s.d.) based on repeated analyses of JMC 475 standard solutions (at 35, 30 or 20 ppb). Replicate analyses of the BHVO-2

reference material gave a $^{176}Hf/^{177}Hf$ value of 0.283108 ± 0.000005 (2 s.d., n=3), in agreement with the reference values of 0.283096 ± 0.000020 (Weis *et al.*, 2005).

The analytical session gave a $^{143}Nd/^{144}Nd$ ratio of 0.512115 ± 0.000007 (2 s.d., n=14), corresponding to an external reproducibility of ± 0.14 ε (2 s.d.) based on repeated analyses of bracketed JNdi-1 standard solution (at 40 ppb). Repeated analyses of the BHVO-2 and BCR-2 reference materials gave respectively a $^{143}Nd/^{144}Nd$ value of 0.512984 ± 0.000006 (2 s.d., n = 3) and 0.512643 ± 0.000005 (2 s.d., n = 3), respectively, agreeing well with published values of 0.512990 ± 0.000010 and 0.512638 ± 0.000015 (Weis *et al.*, 2006).

The Hf isotope data are reported using the standard notation $\varepsilon_{Hf(t)} = [((^{176}Hf/^{177}Hf)_{sample}/(^{176}Hf/^{177}Hf)_{CHUR}) - 1] \times 10^4)$, corrected for the radioactive decay of ^{176}Lu to ^{177}Hf based on Hf and Lu concentrations measured for each sample ($^{176}Lu/^{177}Hf$ = Lu/Hf x 0.1424), the absolute age (t) calculated using the age model of Erbacher *et al.* (2004) and the timescale of Gradstein *et al.* (2012), and the ^{176}Lu radioactive decay constant λ (1.867×10^{-11} an^{-1} ; Söderlund *et al.*, 2004). The initial $^{176}Hf/^{177}Hf$ ratio of the CHondritic Uniform Reservoir was calculated using the present-day CHUR value of 0.282785 and a $^{176}Lu/^{177}Hf$ ratio of 0.0336 (Bouvier *et al.*, 2008).

The Nd isotope data are reported using the standard notation $\varepsilon_{Nd(t)} = [((^{143}Nd/^{144}Nd)_{sample}/(^{143}Nd/^{144}Nd)_{CHUR}) - 1] \times 10^4)$ corrected for the radioactive decay of ^{147}Sm to ^{143}Nd based on measured Nd and Sm concentrations ($^{147}Sm/^{144}Nd$ = Sm/Nd x 0.6049), the absolute age (t) and the ^{147}Sm radioactive decay constant λ (6.54×10^{-12} an^{-1} ; Lugmair & Marti, 1977). The $^{143}Nd/^{144}Nd$ ratio of CHUR was calculated using the present-day value of 0.512630 and a $^{147}Sm/^{144}Nd$ ratio of 0.1960 (Bouvier *et al.*, 2008).

4. Results

4.1. Bulk and clay mineralogy

The bulk sediment assemblage (Fig. 2 ; Supplementary Table 1) is composed of clays (0 to 36%), quartz (0.5 to 28%), K-feldspar (0 to 5%), calcite (14 to 98 %), plagioclase (0 to 11%), opal-CT (0 to 58 %), clinoptilolite (0.6 to 19 %), pyrite (0 to 5 %), gypsum (0 to 10 %) and traces of dolomite (≤ 1 %). From the Turonian to Santonian, a rich assemblage is composed of all the identified minerals. After the Santonian, the proportions of clinoptilolite, pyrite, gypsum and dolomite decrease and these minerals progressively disappeared (Fig. 2). The main mineralogical evolution concerns variations in the carbonate and siliceous mineral content. A net increase of the opal-CT and low-quartz content is indeed observed in the Santonian to Campanian interval balanced by an apparent decrease of calcite following an episode marked by an increase in clinoptilolite (Fig. 2). The plagioclase and K-feldspar proportions also present a slight increase from the Coniacian to the Campanian, then record a decrease from the Campanian to the Maastrichtian as well as the quartz content while the proportions of clay slightly increased (Fig. 2).

Clay mineralogy data show that clay-size fractions at Site 1259 are dominated by smectite (~85 to 100 %), with minor amounts of illite and palygorskite (both up to ~8 %), and traces of kaolinite and chlorite (Fig. 3 , Supplementary Table 1). Note that chlorite contents are negligible (<1 %). Clay mineral assemblages do not present major changes along the studied interval. The Turonian samples present the highest proportions of illite and palygorskite, up to 8%, which then decrease and remain lower than 5% from the Coniacian to the Maastrichtian apart from a slight increase in illite during the Coniacian-Campanian interval (Fig. 3).

4.2. Major elements

Major elements were measured in the bulk sediments and gave a wide range of concentrations (Table 1). The elements content vary from 1.70 to 59.93 % (mean 21.90 %) for SiO_2, from 0.48 to 8.11 % (mean 3.83 %) for Al_2O_3 and from 0.02 to 0.33 % (mean 0.16 %) for TiO_2.

The K_2O content vary from 0.01 to 1.62 % (mean 0.44 %), the CaO content from 12.37 to 52.91 % (mean 31.71 %) and the Na_2O content from 0.03 to 1.63 % (mean 0.82 %). Finally, the content vary from 0.03 to 1.59 % (mean 0.396 %) for P_2O_5, from 0.16 % to 4.30 % (mean 1.33 %) for Fe_2O_3, from 0.01 % to 0.08 % (mean 0.02 %) for MnO, from 0.47 % to 1.46 % (mean 0.76 %) for MgO and from 0 % to 0.03 % (mean 0.01 %) for the Cr_2O_3.

4.3. Hf, Zr and REE concentrations

The rare earth and trace elements concentrations are reported in Table 1. The analysed clay fraction displays zirconium (Zr) concentrations between 42 and 157 ppm that are in the range of modern zircon-poor clay-size fraction (Bayon et al., 2016). Rare Earth Element concentrations of the samples (Table 1) have been normalized to Post-Archean average Australian Shale (PAAS; Taylor et McLennan, 1985), with REE patterns displayed on Fig. 4. Most of the samples present a relatively flat pattern as expected for detrital clays (Fig. 4), that is also highlighted by their position in the "flat" REE pattern domain in a crossplot (Fig.5B) MREE/MREE* (MREE : Middle Rare Earth Elements) versus HREE/LREE (Heavy Rare Earth Elements/Light Rare Earth Elements), except for three samples (at 494.26 m, 494.74 m and 506.05 m) that display a slight enrichment in HREE and a slight negative cerium anomaly (Ce/Ce*) between about 0.5 and 0.7). Figure 5.A presents a crossplot HREE vs Ce/Ce* highlighting the position of these three samples compared to the remaining of the samples

4.4. Hf-Nd isotopes

The $^{143}Nd/^{144}Nd$ and $^{176}Hf/^{177}Hf$ ratios and the $\varepsilon_{Nd(t)}$ and $\varepsilon_{Hf(t)}$ values are provided in Table 2. The Nd isotope composition of studied samples displays unradiogenic values from -13.8 in the Turonian to -15.7 in the Campanian, reaching -17.5 in the late Campanian following a

positive excursion with values up to -12.3 (Figs. 3, 6). A slight increase is observed during the Maastrichtian with values up to -15.6. The Hf isotope composition of the studied samples displays unradiogenic values between -12.2 to -6.0 (Fig. 3, 6). They first decrease from values of about -7.4 during the Turonian to values of about -12.2 in the Coniacian, then increase from the Campanian to the end of the Maastrichtian where they reach values of about -6.1. Finally, calculated $\Delta\varepsilon_{Hf(t)clay}$ values at Demerara Rise decrease from the end of the Turonian to the Santonian – earliest Campanian, from -1.3 to -5.1 (Fig. 3). Then, $\Delta\varepsilon_{Hf(t)clay}$ values increase during the Campanian until the end of Maastrichtian with values up to - 0.1 (Fig. 3).

5. Discussion

5.1. Influence of authigenesis and diagenesis on mineralogical and geochemical signals

Clay mineral assemblages at Site 1259 are dominated by smectite, what is a common feature of upper Cretaceous marine sediment sequences, which were shown to be mainly of detrital origin (Robert, 1981 ; Chamley, 1989). This is further corroborated by TEM observations (Fig. 7.B), which reveal the presence of flaky shape smectite particles, with no evidence of lath-type overgrowths characteristic of clay authigenesis (Clauer *et al.*, 1990). However, three samples at 494.26 m, 494.74 m and 506.05 m (80.25, 83.36 and 89.15 Ma) are marked by a slight negative cerium anomaly, down to 0.53, and slight enrichments in heavy rare earth elements, (Figs. 4, 5) which could possibly indicate the presence of a seawater signal associated with authigenic clay formation (Fagel, 1992 ; Figs. 4, 5).

Interestingly, these three samples presenting some evidence of clay authigenesis formation, althought limited, also yield more radiogenic (less negative) ε_{Nd} values (Fig. 3, 8 ; Table 2).

At Demerara Rise, $\varepsilon_{Nd(t)}$ seawater values inferred from fish tooth ε_{Nd} are quite negative during the late Cretaceous, around -16 on average over most of the interval although excursions toward more radiogenic values have been recorded during Oceanic Anoxic Event

2 (OAE2, Cenomanian-Turonian), up to -8, and at the end of the Maastrichtian (Fig. 8; MacLeod et al., 2008; Martin et al., 2012). Although the origin of the radiogenic excursion of seawater $\varepsilon_{Nd(t)}$ during OAE2 still remains discussed, it has been interpreted as reflecting the input of more radiogenic tethyan seawater at Demerara Rise. As Demerara Rise represented a bathymetric high (Loncke *et al*., 2020), it may have been potentially more affected by changes in oceanic currents than other parts of the margin basins. Unfortunately, no seawater ε_{Nd} data are available at Demerara Rise for the period encompassing the three clay samples that present a slight negative Ce anomaly, a slight HREE enrichment, and more radiogenic $\varepsilon_{Nd(t)}$ values. Thus, it is not possible to determine if this interval was associated with more radiogenic seawater $\varepsilon_{Nd(t)}$ values at Demerara Rise as it was observed for OAE2 and the late Maastrichtian, that could explain a deviation of clay ε_{Nd} toward more radiogenic values if authigenic clays formed at that time and integrated this more radiogenic seawater signal. Alternatively, post-depositional alteration of volcanogenic material linked with active volcanism from the CLIP (Caribbean Large Igneous Province) and/or the Bahamas hot spot (Roddaz *et al.*, 2021) would also result in authigenic smectite formation with a quite radiogenic Nd signature. Sporadic excursions of clay Nd isotope composition toward more radiogenic values have also been reported by Roddaz *et al.* (2021), interpreted as reflecting either an increase in the proportion of radiogenic material eroded from ancient mafic sources exposed on the continent, or as the occurrence of volcanogenic inputs. Such input of mafic/volcanogenic material would be expected to induce an Eu anomaly in the REE spectra of the 3 samples with more radiogenic $\varepsilon_{Nd(t)}$ values, which is not observed here (Fig. 4; supplementary figure 3).

According to the literature, the sediment interval associated with the most radiogenic sample (Core 18 section 7 at 494.26 m ; Fig. 3) also contains a glauconitic level interpreted as an evidence of very low sedimentation rates (Friedrich & Erbacher, 2006 ; Nederbragt *et al.*,

2007 ; März *et al.*, 2009). This condensed interval is also characterized by the hiatus observed between the Coniacian and the Campanian, which marks the lithological transition between claystones and marly-chalks (Fig. 3). This particular event may have been induced by the Santonian-Campanian transgression that led to more open oceanic conditions (Haq, 2014). The observation of smear slides, performed on two samples from the bottom of the core, including the sample presenting the highest (most radiogenic) Nd values, clearly reveals the occurrence of glauconite (Fig. 7.A), hence confirming localized neoformed clay minerals. Low sedimentation rates and a decrease of detrital supply to the site would have favoured the formation of authigenic smectite and glauconite, potentially enhanced by in situ weathering of volcanogenic material deposited during this period.

The presence of glauconite observed in smear slide and previously described in the core (Erbacher *et al.*, 2004), could possibly lead to an overestimation of illite contents as these two clay minerals have overlapping diffraction peaks that cannot be distinguished by XRD analyses. However, smear slide observations show that only some samples of core 18 are marked by the presence of glauconite while the other levels displaying high illite contents (Fig. 3) do not contain glauconite, confirming that most of clays are detrital for the Demerara Rise site. Palygorskite in marine sediments can also be formed during marine authigenic processes, but TEM observations indicate short and broken palygorskite fibres characteristic of a detrital origin (Fig. 7.B).

Apart from the 3 samples with some evidence of clay authigenesis and partial incorporation of a seawater signal, all other clay-size fractions present flat shale-normalized rare earth element (REE) patterns and an absence of any Ce anomaly (Ce/Ce* above 0.7 ; Roddaz *et al.*, 2021 ; Fig. 4, 5) and corresponds to the “Shale” fields in figure 5.B , thereby indicating a detrital origin for the late Cretaceous clays at Demerara Rise, as already pointed out by Roddaz *et al.* (2021). This is also coherent with the interpretation of März *et al.* (2009),

who showed, based on major and trace element composition, that detrital sediments deposited at the Demerara Rise during the late Cretaceous were essentially derived from the erosion of the adjacent Guiana-Suriname margin. Overall, clay minerals at Site 1259 appear mostly inherited from nearby continental landmasses, with only limited and sporadic influence of authigenesis (i.e. glauconite, volcanogenic smectite) along the studied sediment sequence.

In the bulk sediment, a net increase in quartz abundance also appears in the Santonian-Campanian interval. However, this increase is also matched by higher opal-CT contents (up to 58% of the bulk sediment, Fig. 2). Quartz may also have a marine biogenic origin by transformation of opal-CT during early diagenesis (associated to temperature lower than 60°C) in marine sequence around 400 meters burial depth (Hesse, 1988). Thus, its concomitant evolution with opal-CT suggests that the increase of quartz is likely associated to biogenic processes and may in this case correspond to microquartz associated to opal-CT both deriving from opal-A (Riech & von Rad, 1979; Hesse, 1988). It has also been reported that calcareous sediments favour the direct transformation of opal-A into quartz while transformation of opal-CT into quartz is enhanced if detrital quartz is present (Hesse, 1988), which may explain the net increase of quartz in the Santonien-Campanien. For this interval, sediment is probably composed of mixed detrital and biogenic microquartz, impeding the use of quartz content to track variations in detrital inputs. Zeolites (i.e. clinoptilolite, Fig. 2) and opal-CT are also formed authigenically by dissolution of amorphous SiO_2 most likely derived from dissolution-reprecipitation of siliceous organisms (März et al., 2009). We have therefore calculated the ratio (Opal+Clinoptilolite)/Calcite ((O+C)/Ca ; Fig. 8) in order to track the variability of marine primary productivity, as it was demonstrated that clinoptilolite was a good proxy of enhanced biogenic silica productivity (e.g. Karpoff et al., 2007).

5.2. Sources and detrital material provenance

The fine-grained detrital material that is eroded from the exposed continental surface and subsequently transported by rivers is assumed to provide a Nd isotopic composition representative of the corresponding catchment areas (Goldstein *et al.*, 2003; Bayon *et al.*, 2015). In our dataset, apart from 3 samples showing some evidence of authigenic clays that will not be considered further to discuss the evolution of the chemical weathering, all other studied clay-size fractions at Site 1259 present geochemical and petrographical features typical of a detrital origin. Isotopic geochemistry of these sediments can therefore be used to track the provenance of the upper Cretaceous sediments deposited on Demerara Rise and to reconstruct the evolution of paleoenvironments in corresponding source regions.

To constrain sediment provenance, we use the regional ε_{Nd} compilation of detrital sources published by Roddaz *et al.* (2021), applying to their published $\varepsilon_{Nd(0)}$ values the same age correction than to our own samples at 83 Ma in order to compare them to our dataset (Fig. 1.B).

The units forming the Guiana Craton display the most unradiogenic values (Fig. 1.B). Three units can be distinguished: 1) the Archean Amapa & Imataca granitoids (AAIG), with an average $\varepsilon_{Nd(t)}$ value of -30.4 (from -41.5 to -1.5; 2σ = 17.2); 2) the Paleoproterozoic granitoids, gneiss and felsic volcanism (PGGF), with an average $\varepsilon_{Nd(t)}$ value of -22.2 (from -41.5 to 30.5; 2σ = 17.2), and 3) the Paleoproterozoic high-grade granulite belts (PHGB), with an average $\varepsilon_{Nd(t)}$ value of -19.8 (from -35.4 to -1.8; 2σ = 16.2). The overlying Mesoproterozoic granites (MG) present an average $\varepsilon_{Nd(t)}$ value of -17.3 (from -20.0 to -14.5; 2σ = 3.9). Finally, three different sources are characterized by more radiogenic values: the Greenstone Belt (GB) and the Paleoproterozoic mafic intrusions (PMI) yielding values around -7.1 (from -17.6 to 4.3; 2σ = 13.2) and the Jurassic mafic dykes (JMD) presenting values around 1.0 (from -4.1 to -6.0; 2σ = 5.9).

Our detrital clay $\varepsilon_{Nd(t)}$, which range between -17.5 and -14 (Figs. 3, 8) with a mean value of -16.08 ± 0.91 (1σ), do not display any particular trend downcore (Table 2). They also agree well with those reported by Roddaz *et al.* (2021) for a more proximal site, between about -20 and -13.5 (Fig. 8). The peripheral regions of the Guiana Shield bordering the Atlantic margin are mainly composed of Paleoproterozoic granitoids and gneisses (PGGF; Fig. 1.B) that represented the main source of the detrital material brought to Site 1259 during the late Cretaceous, with a potential additional contribution of more radiogenic greenstone belts (GB) (Roddaz et al., 2021).

The slightly more radiogenic composition of clays during the Turonian could reflect a larger contribution of material derived from the greenstone belts (-7.1; Fig.1.B) or from Jurassic mafic dykes (1.0 ; Fig. 1.B), which would have decreased from the Turonian to the Campanian. Apart from the likely decrease in the contribution of relatively radiogenic rocks to the detrital fraction deposited at Site 1259 from the Turonian to the Coniacian, and a slight increase in the Maastrichtian, no major change in the source of sediments is thus depicted in the Nd isotope signal.

The detrital fraction of the studied sediments thus mainly arises from the weathering and erosion of the Guiana craton. To some extent, the evolution in relative proportions of primary clay minerals (illite, chlorite) versus secondary clay minerals (smectite, kaolinite) can provide information on tectonic uplift patterns along continental margins, as newly forming topographic reliefs naturally increase proportions of primary mineral assemblages. Indeed illite and chlorite are primary clay minerals resulting from the erosion of igneous, metamorphic and old sedimentary rocks showing limited degree of chemical weathering intensity. They typically form under relatively dry climate conditions or in active tectonic settings characterized by limited chemical weathering processes (Chamley, 1989). Under more humid climate, (semi-arid or alternation of wet and dry seasons) enhanced chemical

weathering of silicate minerals typically leads to smectite formation in soils (bisialitisation ; Chamley, 1989 ; Ruffell *et al.*, 2002; Deconinck *et al.*, 2019). Sub-arid or seasonally arid conditions can also favour the formation of palygorskite that precipitates in evaporative basins, such as inland seas, lakes or other peri-marine environments (Callen, 1984 ; Chamley, 1989 ; Daoudi 2004). Finally, kaolinite is commonly associated to hot and wet climate, intense chemical weathering and optimal drainage conditions (Chamley, 1989; Thiry, 2000; Ruffell *et al.*, 2002; Dera *et al.*, 2009).

In northeastern South America, warm and humid conditions most likely prevailed during the late Cretaceous, as inferred from combined field data and climate model investigations (Théveniaut *et al.*, 2002 ; Hay *et al.*, 2012), coherent with the observed dominance of pedogenic smectite at the Demerara Rise. The fact that only limited amounts of kaolinite were detected during the Maastrichtian at this equatorial site raises questions. It is possible that climate was not sufficiently humid throughout the year to provide either monosialitisation or allitisation (e.g. bauxite formation) leading to abundant kaolinite-rich deposits. However, this latter hypothesis appears in contradiction with evidence of an extensive lateritization phase on the Guiana Shield during the late Cretaceous (Théveniaut *et al.*, 2002). Alternatively, the absence of kaolinite at the studied site could reflect a differential settling effect in seawater, because kaolinite grains are coarser than smectite particles (Godet *et al.*, 2008). While kaolinite was probably formed onshore in the lateritic soils encountered on the Guiana Shield, its net export to the nearby continental margins could have been hampered by preferential deposition in the flooded shelf area (März *et al.*, 2009). Conversely, due to their smaller size, smectite was likely formed preferentially in flatter continental areas and would have been transported to more distal marine environments. Such a gradient in smectite vs kaolinite proportions due to differential settling from the continental plateau to the oceanic basins is commonly observed in modern environments (Chamley, 1989; Gingele et al., 1998).

Similarly, primary coarser clay minerals such as illite and chlorite were most likely preferentially deposited in proximal flooded shelf areas and in the GS and FOZ basins rather than on the topographic high of the Demerara Plateau (Fig. 1.B), that could explain the low proportions of primary clay minerals at the site. This would be coherent with geochemical data and sedimentary fluxes reported by März *et al.* (2009) and Loparev *et al.* (2021), indicating a sediment starvation of the Demerara Plateau at this time and preferential deposition of coarse sediments in the flooded shelf area and in the GS and FOZ basins. Such a differential setting effect, resulting in the preferential transport via surface currents of small-size smectite particles to Demerara Rise site, could explain the large dominance of smectite in studied clay fractions (85 to 100% ; Fig. 2).

Due to the very high proportions of smectite relative to other clay minerals, the variation in abundance of clay minerals must be interpreted with caution. The co-evolution of illite and palygorskite contents during the Turonian may indicate reworking of clay minerals derived from old sedimentary and igneous rocks or, alternatively, may be linked to enhanced eolian activity, as it is known that palygorskite can be easily transported by winds in sub-arid evaporitic environments (Pletsch *et al.*, 1996 ; Knidiri *et al.*, 2014). In this case, the higher palygorskite proportions recorded at Demerara Rise could indicate the existence of more arid episodes during the Turonian. Alternatively, palygorskite and illite could also come from the erosion of old Mesozoic sediments derived from sedimentary basins bordering the Guiana Craton, including the Takutu Basin (Fig. 1B). Indeed, palygorskite is commonly associated with the Jurassic and early Cretaceous evaporitic lacustrine environments that formed during the opening of the Central Atlantic (Crawford *et al.*, 1984 ; Castro *et al.*, 2021). The erosion of such Mesozoic basins during the Turonian would be consistent with the pre-Coniacian catchment areas defined by Roddaz *et al.* (2021) based on ε_{Nd} and trace element abundances. In any case, these minerals represent a very low proportion of the total clay content that is

mainly dominated by detrital contemporaneous smectites and should not impact Nd-Hf isotopic values.

During the Turonian, the higher content of palygorskite and illite, if eroded from old Mesozoic sediments, could be indicative of higher erosion rates. A slight increase in illite proportions is also recorded during the Coniacian-Campanian interval, with a maximum value around 80 Ma ago, coupled with slightly higher feldspar contents in the bulk sediment (Fig. 2). This is also illustrated by the variations of the (I+C)/S and Feld/Clays ratio in figure 8. Although discrete, these features may reflect enhanced mechanical erosion promoting both primary silicate minerals (e.g. feldspar ; Figs. 2, 8) and coarse and primary clay minerals (e.g. illite) during an uplift phase. This would be consistent with the timing of the main pulses of tectonic activity and higher sedimentation rates in the GT and FOZ basins during this interval (Sapin *et al.*, 2016 ; Loparev *et al.*, 2020 ; Fig. 1.B). Presumably, at that time, enhanced tectonic activity along the northeastern South American margin was accompanied by enhanced erosional fluxes and nutrient export to seawater, which could also have driven enhanced biosiliceous marine productivity inferred from the (O+C)/Ca ratio (Fig. 8). This mechanism may explain the concomitant increase of biogenic phases and the detrital input during the Campanian in relation to the main tectonic pulse, although a role of aerial explosive volcanism activity as a potential source of siliceous material cannot be excluded (Frogner *et al.*, 2001 ; Stokke *et al.*, 2021).

5.3. Evolution of chemical weathering linked to climate and tectonic.

The identification of distinct uplift pulses during the Turonian and Campanian-to-early Maastrichtian period in the studied area (Fig. 9, Sapin *et al.*, 2016) has provided evidence for a major tectonic phase affecting the eastern South American margin at that time. Argon/argon (Ar/Ar) dating of the late Cretaceous planation surface S0 (McConnell, 1968 ; Sapin *et al.*,

2016) yields an age of 71 Ma, while apatite fission track data (AFTA) indicate ages of 77 ± 3 Ma, 83 ± 5 Ma and 99 ± 9 Ma for the periods of enhanced regional tectonic activity (Fig. 9 ; Sapin *et al.*, 2016). In the FOZ basin, the highest terrigenous accumulation rates occurred during the Campanian-Maastrichtian interval (Loparev *et al*., 2021), associated with the main uplift phase, while in the GS basin, Roddaz et al. (2021) shows an increase in sedimentation rates during the Santonian.

In order to track the impact of tectonic uplift, inferred from Ar/Ar dating of planation surfaces and AFTA, on the evolution of chemical weathering intensity in NE South America, we now consider Nd and Hf isotope data measured in the clay-size fraction. The combined use of Nd and Hf isotopes in fine-grained sediment records is a powerful proxy to track changes in continental chemical weathering (Bayon *et al.*, 2012 ; Fontanier *et al.*, 2018 ; Corentin *et al.*, 2022; Bayon et al., 2022). While the Lu-Hf and Sm-Nd isotopic systems behave similarly during magmatic processes, defining a so-called «Terrestrial array» in most igneous and sedimentary rocks (Fig. 6, Vervoort *et al.*, 1999 ; Vervoort *et al.*, 2011), they are decoupled during Earth surface processes such as chemical weathering and sediment transport (Vervoort *et al.*, 1999 ; Bayon *et al.*, 2016 ; Garçon *et al.*, 2013 ; Garçon & Chauvel, 2014 ; Chauvel *et al.*, 2014). This decoupling is partly due to mineral sorting, which causes preferential enrichment of zircons in the coarse-grained sediment fraction, characterized by high Hf concentrations and very low ε_{Hf} (unradiogenic) compositions (Vervoort *et al.*, 1999 ; Chauvel *et al.*, 2014). By contrast, clay-size fractions of sorted sediments are typically depleted in zircons and hence are systematically shifted towards more radiogenic ε_{Hf} values compared to coarser sediment fractions, defining a so-called « clay array » (Zhao et al., 2014; Bayon *et al.*, 2016 ; Fig. 6). Additionally, the mineral phases most susceptible to chemical weathering on continents are typically enriched in Lu relative to Hf, hence leading to the preferential release of radiogenic Hf during weathering (Bayon *et al.*, 2006 ; Bayon *et al.*,

2016 ; Dausmann *et al.*, 2019). Upon formation of secondary clay minerals in soils, a fraction of dissolved radiogenic Hf can be incorporated into clays (Bayon *et al.*, 2016). As a result, clay-size fractions derived from intensively weathered soils are associated with more radiogenic clay ε_{Hf} signatures, which partly reflect an increase in the relative proportion of secondary clay minerals (high ε_{Hf}) relative to unweathered primary detrital mineral (low ε_{Hf}). In fine-grained sediment records, a more intense chemical silicate weathering hence results in a vertical departure of clay ε_{Hf} from the « clay array », noted $\Delta\varepsilon_{Hf}$ (Fig. 6 ; Bayon *et al.*, 2016). Note that $\Delta\varepsilon_{Hf}$ has not been calculated for the 3 samples presenting evidence of a seawater imprint on the clay fraction Nd isotope signal linked to the presence of authigenic clays.

The analysed clay fraction presents low zirconium (Zr) concentrations (between 42 and 157 ppm), in the range of modern clay-size fractions separated from river sediments (Bayon *et al.*, 2015). Additionally, there is no significant correlation between ε_{Hf} values and Zr concentrations (R^2 = 0.23 ; Supplementary Fig. 1), nor between $\Delta\varepsilon_{Hf}$ and Zr concentrations. This observation indicates that the $\Delta\varepsilon_{Hf(t)clay}$ evolution of studied clays is not controlled by the presence of residual zircons in the isolated < 2µm sediment fraction, but rather reflects variations in silicate weathering intensity of the catchment area.

The close correspondance of $\Delta\varepsilon_{Hf\ clay}$ with climatic parameters and with the chemical index of alteration (CIA) observed in clays recovered from rivers receiving weathering products from source rocks of various nature suggests a minor influence of lithology on $\Delta\varepsilon_{Hf}$ (Bayon *et al.*, 2016). At Site 1259, the limited $\varepsilon_{Nd(t)}$ variations through the studied interval points to the absence of major change in the lithologies of the sediment source, while $\Delta\varepsilon_{Hf(t)clay}$ increases quite markedly. Most importantly, no correlation is depicted between $\varepsilon_{Nd(t)}$ and $\Delta\varepsilon_{Hf(t)}$, demonstrating that variations in $\Delta\varepsilon_{Hf(t)}$ are not controlled by lithology variations of the source rock at this site (Supplementary figure 2).

Calculated $\Delta\varepsilon_{Hf(t)clay}$ values at Demerara Rise are thus interpreted hereafter to reflect the evolution of chemical weathering intensity, with the depicted decrease in $\Delta\varepsilon_{Hf(t)clay}$ pointing to a decrease in weathering of surrounding catchment regions from the end of the Turonian to the Santonian or beginning of Campanian (Fig. 8 ; Bayon *et al.*, 2016). Then, from Campanian to the end of Maastrichtian, a marked increase in regional silicate weathering intensity is recorded (Figs. 3, 8). Superimposed on this trend, a slight decrease in $\Delta\varepsilon_{Hf(t)clay}$ values, reflecting an interval of lower weathering intensity, is also recorded during the late Campanian and Early Maastrichtian, of about 2.0 (Figs. 3, 8).

The Chemical Index of Alteration (CIA) has also been widely used to track changes in chemical weathering (e.g. Young & Nesbitt, 1999; Roddaz et al., 2006), as it provides an estimation of the degree of mobile element depletion relative to immobile elements during chemical weathering (Nesbitt & Young, 1982), although this proxy is known to be influenced by sediment source and mineral sorting (Fantasia *et al.*, 2019). At Site 1259, no major change in sediment provenance occurred during the late Cretaceous but Campanian sediments are marked by higher opal-CT and quartz contents increasing the concentrations of silicon and thus decreasing aluminium relative proportions. The CIA value calculated for the two samples exhibiting the highest contents of biogenic minerals is very low (<50), hence suggesting a dilution effect by Si impeding its use as a weathering proxy in the interval marked by high opal-CT and quartz contents (Fig. 8). The pronounced increase of the CIA that subsequently follows (from 56 to 74) is however not associated to concomitant change in opal-CT and quartz contents, nor in sediment sources as ε_{Nd} values remain quite constant, and thus could reflect an increase of chemical weathering intensity from the middle Campanian to the late Maastrichtian. This interpretation would be in agreement with the increase depicted in $\Delta\varepsilon_{Hf(t)clay}$.

Over long timescales, the evolution of continental chemical weathering is thought to be driven mostly by climate and tectonics. Increasing temperature and precipitation favour the kinetics of silicate weathering reactions and increase wetting of reactive mineral surface areas, enhancing silicate mineral dissolution rates (White & Blum, 1995 ; Berner *et al.*, 1983 ; Gaillardet *et al.*, 1999 ; Barron & Washington, 1985 ; Pierrehumbert, 2002). Active tectonic settings associated with high denudation rates and mechanical erosion can also promote high chemical weathering rates by favouring both the disaggregation of silicate minerals and renewing the exposure of fresh rock surfaces available to weathering. The relationship between mechanical erosion and chemical weathering is however not straightforward. Under supply-limited weathering conditions, the rate of chemical weathering is proportionally related to denudation rates (Raymo *et al.*, 1988 ; West *et al.*, 2005 ; Gabet & Mudd, 2009). In contrast, under kinetically-limited weathering conditions, detrital material is removed too fast from the regolith, and higher denudation rates are not accompanied by higher chemical weathering rates (West, 2005 ; Gabet and Mudd, 2009).

The evolution of chemical weathering intensity depicted by $\Delta\varepsilon_{Hf(t)clay}$ matches relatively well the evolution of ocean temperature inferred from both planktic foraminifera at Demerara Rise (Fig. 8 ; Bornemann *et al.*, 2008) and the global benthic foraminiferal $\delta^{18}O$ reconstruction (Fig. 8 ; Friedrich *et al.*, 2012). Chemical weathering in northeastern South America markedly decreased during the climate cooling recorded from the end of the Turonian to the early Campanian, suggesting a climatic control of this evolution, as lower temperature reduces silicate weathering reactions (Fig. 8 ; White and Blum, 1995). Similarly, the cooling recorded in the latest Campanian and early Maastrichtian appears to be also associated with a decrease, albeit more limited, of continental weathering intensity (Fig. 8). However, if a slight warming is observed in the foraminiferal $\delta^{18}O$ dataset during the middle and late Campanian, global temperature remains markedly lower in the late Campanian and

Maastrichtian than during the Turonian, when chemical weathering markedly increased as inferred from $\Delta\varepsilon_{Hf(t)clay}$ values exceeding those recorded for the Turonian. Therefore, for the middle Campanian to Maastrichtian interval, the evolution of global temperature is unlikely to fully account for our chemical weathering record, hence requiring an additional process resulting in enhanced silicate weathering. Throughout the studied interval, there is no evidence for marked changes in the amount of precipitation; nearby continental regions remained within a humid climatic belt as documented by the occurrence of laterites and bauxites throughout the late Cretaceous (Théveniaut *et al.*, 2002 ; Hay, 2012). Consequently, we infer that the observed marked increase in chemical weathering was presumably not induced by a regional climate shift towards wetter conditions.

As mentioned above, during the Campanian, the northeastern South American margin experienced several tectonic pulses that led to the uplift of the craton (McConnell, 1968 ; Potter, 1997 ; Harman *et al*. 1998 ; Morais Neto et al. 2009 ; Peulvast and Bétard 2015 ; Sapin *et al.*, 2016 ; Monteiro *et al*. 2018). This uplift most likely drove enhanced mechanical erosion as suggested by the slight increase in illite and feldspar at Site 1259, which, in a permanently humid climatic belt, could have been associated with more intense silicate weathering as well (West, 2005 ; Gabet & Mudd, 2009). The occurrence of a major uplift phase concomitant with a pronounced $\Delta\varepsilon_{Hf(t)clay}$ increase (Fig. 8), with values exceeding those recorded in the Turonian despite markedly lower temperatures, strongly points towards tectonics as being the main driver of chemical weathering variability in northeastern South America during the middle Campanian to Maastrichtian interval. By contrast, from the end of the Turonian to the early Campanian interval, when tectonic activity was reduced, climate was instead the main parameter controlling the evolution of chemical weathering in the study area.

Altogether, our data thus suggest the dominant control of tectonics on continental weathering when occurring under wet climate conditions, with a more limited role of

temperature. These findings complement previous inferences based on Site 356 offshore Brazil, which showed that under semi-arid climate conditions, chemical weathering did not respond to the tectonic uplift of the Brazilian margin until local climate evolved toward more hydrolysing conditions (Corentin *et al.*, 2022). Surprisingly, the $\Delta\varepsilon_{Hf(t)clay}$ values recorded at site 1259 are negative for the most part, with values down to -5 which are observed at present in cold and dry climatic zones, although values recorded during the latest Campanian and Maastrichtian, up to 1, are observed in modern tropical humid belts (Bayon et al. (2016). By contrast, higher $\Delta\varepsilon_{Hf(t)clay}$ values are recorded at site 356 located in a semi-arid climatic zone (Fig. 6). This apparent discrepancy may further point to a preponderant role of tectonics on silicate weathering through supply of fresh minerals exposed to weathering processes, favoured by enhanced physical erosion. At site 1259, in the context of relative tectonic quiescence during the interval recording the most negative values, these low $\Delta\varepsilon_{Hf(t)clay}$ values may reflect the existence of limited chemical weathering under supply-limited conditions (West et al., 2005; Gabet and Mudd, 2009), impeded by low physical erosion rates reducing the renewed supply of fresh minerals to weathering processes. Alternatively, the correspondence between absolute $\Delta\varepsilon_{Hf(t)clay}$ values with climatic zones may have been different in the overall greenhouse climate mode of the late Cretaceous than from our modern icehouse climate mode, in which they have been established. Although the significance of absolute $\Delta\varepsilon_{Hf(t)clay}$ values still needs further investigation, our study highlights the potential of relative variations in $\Delta\varepsilon_{Hf(t)clay}$ at a specific site remains to infer relative changes in silicate chemical weathering at a local scale.

Variations in continental weathering can also impact global climate through atmospheric CO_2 drawdown by silicate weathering reactions. Combined Hf-Nd and clay mineralogical data from Site 356 offshore Brazil have recently highlighted an increase in silicate weathering along the Brazilian margin from the Santonian onward, which coincided with an acceleration

of the late Cretaceous global climate cooling (Friedrich *et al*., 2012). At Site 1259, the marked increase in chemical weathering affecting the northeastern South American margin initiated during the middle Campanian, appears post-dating the main global cooling phase inferred from the benthic foraminiferal $\delta^{18}O$ record. While the tectonic uplift of the northern South American margin and its impact on chemical weathering hence could not have triggered the long-term climate cooling during the late Cretaceous, it is possible that weathering-driven atmospheric CO_2 drawdown contributed to maintaining cooler conditions in the late Campanian and Maastrichtian. Altogether, the data from Site 356 (Corentin *et al*., 2022) offshore southeastern Brazil, and the new data from Site 1259 at Demerara Rise (this study) highlight the possible importance of the late Cretaceous uplift of the Eastern South American margin on the long-term cooling recorded during this period.

Conclusion

The new $\Delta\varepsilon_{Hf(t)clay}$ proxy based on combined Nd-Hf isotope measurements of clay-size fractions was applied to a sediment record from Demerara Rise in order to the reconstruct the evolution of continental silicate weathering intensity at the northeastern South American margin during the late Cretaceous.

The depicted evolution of $\Delta\varepsilon_{Hf(t)clay}$ seems to show a co-variation of chemical weathering with global climate, except during the middle Campanian to Maastrichtian interval when inferred chemical weathering intensity was higher than during the Turonian despite cooler climate conditions. During this Campanian-to-Maastrichtian period, our proxy record indicates that major tectonic uplift of the northeastern South American margin was accompanied by an intensification of chemical weathering. By contrast, from the end of the Turonian to the early Campanian, i.e. a period characterized by reduced tectonic activity, the

evolution of continental weathering in northern South America was mostly influenced by climate.

Our dataset brings new constraints on the combined influence of tectonics and climate in driving the long-term evolution of continental chemical weathering through time. Under persistent tropical climate conditions, tectonics appears to play a major role in controlling silicate weathering, while the impact of temperature appears less prominent. Overall, the response of chemical weathering to tectonic uplift along the eastern margin of South America inferred from our proxy data suggests that this major tectonic event could have partially contributed to the late Cretaceous cooling through weathering-driven atmospheric CO_2 drawdown.

Data availability

All the data are provided in the supplementary materials attached to this paper.

Acknowledgments

We thank IODP for providing access the material. IODP France and ANR RISE funded the project. We also thank Rémi Chassagnon (Laboratory ICB, University of Burgundy) and INRAe of Dijon, Ludovic Bruneau of the Biogéosciences Laboratory and GISMO analytical Platform (University of Burgundy), Marie-Laure Rouget and Bleuenn Gueguen of the Pôle Spectrométrie Océan (Brest) and Philippe Telouk of the ENS Lyon for their analytical support.

References

Barrat, J.A., Keller, F., Amossé, J., Taylor, R.N., Nesbitt, R.W., Hirata, T. 1996. Determination of Rare Earth Elements in Sixteen Silicate Reference Samples by Icp-Ms After Tm Addition and Ion Exchange Separation. Geostandards Newsletter 20, 133–139.

Barron, E. J., Washington, W. M. 1985. Warm Cretaceous climates: High atmospheric CO_2 as a plausible mechanism. In: The carbon cycle and atmospheric CO_2 : Natural Variations, Archean To present (Geophys Monogr. 32) AGU, edited by Sundquist, E. and Broeker, W., 546–553, Washington DC, 984-999.

Basile, C., Maillard, A., Patriat, M., Gaullier, V., Loncke, L., Roest, W., Mercier de Lépinay, M., Pattier, F. 2013. Structure and Evolution of the Demerara Plateau, Offshore French Guiana: Rifting, Tectonic Inversion and Post-Rift Tilting at Transform-Divergent Margins Intersection. Tectonophysics, Basin Dynamics, 591 (April): 16-29.

Bayon, G., German, C.R., Boella, R.M., Milton, J.A., Taylor, R.N., Nesbitt, R.W. 2002. An improved method for extracting marine sediment fractions and its application to Sr and Nd isotopic analysis. Chemical Geology 187, 179–199.

Bayon, G., Vigier, N., Burton, K.W., Agnès Brenot, J.C., Etoubleau, J., Chu, N.-C. 2006. The control of weathering processes on riverine and seawater hafnium isotope ratios. Geology 34, 433–436.

Bayon, G., Barrat, J.A., Etoubleau, J., Benoit, M., Bollinger, C., Révillon, S. 2009b. Determination of Rare Earth Elements, Sc, Y, Zr, Ba, Hf and Th in Geological Samples by ICP-MS after Tm Addition and Alkaline Fusion. Geostandards and Geoanalytical Research 33, 51–62.

Bayon, G., Dennielou, B., Etoubleau, J., Ponzevera, E., Toucanne, S., Bermell, S. 2012. Intensifying Weathering and Land Use in Iron Age Central Africa. Science 335, 1219–1222.

Bayon, G., Toucanne, S., Skonieczny, C., André, L., Bermell, S., Cheron, S., ... & Barrat, J. A. (2015). Rare earth elements and neodymium isotopes in world river sediments revisited. *Geochimica et Cosmochimica Acta*, *170*, 17-38.

Bayon, G., Skonieczny, C., Delvigne, C., Toucanne, S., Bermell, S., Ponzevera, E., André, L. 2016. Environmental Hf–Nd isotopic decoupling in World river clays. Earth and Planetary Science Letters 438, 25–36.

Bayon, G., Bindeman, I. N., Trinquier, A., Retallack, G. J., & Rekker, A. (2022). Long-term evolution of terrestrial weathering and its link to Earth's oxygenation. *Earth and Planetary Science Letters*, *584*, 117490.

Berner, R. A., Lasaga, A. C., Garrels, R. M. 1983. The carbonate-silicate geochemical cycle and its effect on atmospheric carbon dioxide over the past 100 million years, Am. J. Sci. 283, 641-683.

Bornemann, A., Norris, R. D., Friedrich, O., Beckmann, B., Schouten, S., Damsté, J. S. S., Vogel, J., Hofmann, P., Wagner, T. 2008. Isotopic Evidence for Glaciation During the Cretaceous Supergreenhouse. Science 319, 189-192.

Bouvier, A., Vervoort, J.D., Patchett, P.J. 2008. The Lu–Hf and Sm–Nd isotopic composition of CHUR: Constraints from unequilibrated chondrites and implications for the bulk composition of terrestrial planets. Earth and Planetary Science Letters 273, 48–57.

Callen, R.A. 1984. Clays of the palygorskite-sepiolite group: Depositional environment, age and distribution. In Singer, A., Galan, E. (Eds.) Palygorskite-sepiolite occurrences, genesis and uses. Dev. Sedimentol. 37. Elsevier Sci. Publ. Co., Amsterdam, 1-37.

Castro, R., Giorgioni, M., de Souza, V., Ramos, M., Feitoza, L. M., Dino, R., Antonioli, L. 2021. Facies analysis, petrography, and palynology of the Pirara Formation (Upper Ju-

rassic-Lower Cretaceous) - Tacutu Basin (Roraima, Brazil). Journal of South American Earth Sciences 112, 103574.

Chamley, H. 1989. Clay sedimentology ed. Springer-Verlag Berlin Heidelberg GmbH.

Chauvel, C., Garçon, M., Bureau, S., Besnault, A., Jahn, B., Ding, Z. 2014. Constraints from loess on the Hf–Nd isotopic composition of the upper continental crust. Earth and Planetary Science Letters 388, 48–58.

Chu, N.-C., Taylor, R.N., Chavagnac, V., Nesbitt, R.W., Boella, R.M., Milton, J.A., German, C.R., Bayon, G., Burton, K. 2002. Hf isotope ratio analysis using multi-collector inductively coupled plasma mass spectrometry: an evaluation of isobaric interference corrections. J. Anal. At. Spectrom. 17, 1567–1574.

Clauer, N., O'Neil, J.R., Bonnot-Courtois, C., Holtzapffel, T. 1990. Morphological, Chemical, and Isotopic Evidence for an Early Diagenetic Evolution of Detrital Smectite in Marine Sediments. Clays Clay Miner. 38, 33–46.

Corentin, P., Pucéat, E., Pellenard, P., Freslon, N., Guiraud, M., Blondet, J., Adatte, T., Bayon, G. 2022. Hafnium-neodymium isotope evidence for enhanced weathering and uplift-climate interactions during the Late Cretaceous. Chemical Geology 591, 12074.

Crawford, F.D., Szelewski, C.E., Alvey, G.D. 1984. Geology and exploration in the Takutu graben of Guyana. J. Pet. Geol. Beaconsfield, 8 (1), 5-36.

Cullers, R. L. 2000. The Geochemistry of Shales, Siltstones and Sandstones of Pennsylvanian Permian Age, Colorado, USA: Implications for Provenance and Metamorphic Studies. Lithos 51 (March): 181-203.

Daoudi, L. 2004. Palygorskite in the uppermost Cretaceous–Eocene rocks from Marrakech High Atlas, Morocco. Journal of African Earth Sciences, Key Points on African Geology 39, 353–358.

Dausmann, V., Gutjahr, M., Frank, M., Kouzmanov, K., Schaltegger, U. 2019. Experimental evidence for mineral-controlled release of radiogenic Nd, Hf and Pb isotopes from granitic rocks during progressive chemical weathering. Chemical Geology, 507, 64-84.

Deconinck, J. F., Hesselbo, S. P., Pellenard, P. 2019. Climatic and sea level control of Jurassic (Pliensbachian) clay mineral sedimentation in the Cardigan Bay Basin, Llanbedr (Mochras Farm) borehole, Wales. Sedimentology 66 (7), 2769-2782.

Dera, G., Pellenard, P., Neige., P., Deconinck, J. F., Pucéat, E., Dommergues, J. L. 2009. Distribution of clay minerals in Early Jurassic Peritethyan seas : palaeoclimatic significance inferred from multiproxy comparisons. Palaeogeography, Palaeoclimatology, Palaeoecology 271 (1-2), 39-51.Engelmann de Oliveira, C.H., Jelinek, A.R., Chemale, F., Cupertino, J.A. 2016. Thermotectonic history of the southeastern Brazilian margin: Evidence from apatite fission track data of the offshore Santos Basin and continental basement. Tectonophysics 685, 21–34.

Erbacher, J., Mosher, D.C., Malone, M.J. 2004. Shipboard scientific party. Proc. ODP. In. Reports, vol. 207.

Erbacher, J., Friedrich, O., Wilson, P.A., Birch, H., Mutterlose, J. 2005. Stable organic carbon isotope stratigraphy across Oceanic Anoxic Event 2 of Demerara Rise, western tropical Atlantic. Geochem. Geophys. Geosyst. 6, Q06010.

Fagel, N., André, L., Chamley, H., Debrabant, P., Jolivet, L. 1992. Clay sedimentation in the Japan Sea since the Early Miocene: influence of source-rock and hydrothermal activity. Sedimentary Geology 80, 27–40.

Fantasia, A., Adatte, T., Spangenberg, J.E., Font, E., Duarte, L.V., Föllmi, K.B. 2019. Global versus local processes during the Pliensbachian–Toarcian transition at the Peniche GSSP, Portugal: A multi-proxy record. Earth-Science Reviews 198, 102932.

Fontanier, C., Mamo, B., Toucanne, S., Bayon, G., Schmidt, S., Deflandre, B., Dennielou, B., Jouet, G., Garnier, E., Sakai, S., Lamas Ruth, M., Duros, P., Toyofuku, T., Salé, A., Belleney, D., Bichon, S., Boissier, A., Chéron, S., Pitel, M., Roubi, A., Rovere, M., Grémare, A., Dupré, S., Jorry, S. 2018. Are deep-sea ecosystems surrounding Madagascar threatened by land-use or climate change? Deep Sea Research Part I: Oceanographic Research Papers 131, 93-100.

Frank, M., 2002. Radiogenic Isotopes: Tracers of Past Ocean Circulation and Erosional Input. Reviews of Geophysics 40, 1-38.

Friedrich, O., Erbacher, J. 2006. Benthic foraminiferal assemblages from Demerara Rise (ODP Leg 207, western tropical Atlantic): Possible evidence for a progressive opening of the Equatorial Atlantic Gateway: Cretaceous Research 27, 377–397.

Friedrich, O., Norris, R.D., Erbacher, J. 2012. Evolution of middle to Late Cretaceous oceans — A 55 m.y. record of Earth's temperature and carbon cycle. Geology 40, 107–110.

Frogner, P., Gíslason, S. R., Oskarsson, N. 2001. Fertilizing potential of volcanic ash in ocean surface water. Geology 29 (6), 487-490.

Gabet, E.J., Mudd, S.M. 2009. A theoretical model coupling chemical weathering rates with denudation rates. Geology 37, 151–154.

Gaillardet, J., Dupré, B., Louvat, P., Allègre, C.J. 1999. Global silicate weathering and CO_2 consumption rates deduced from the chemistry of large rivers. Chemical Geology. 159, 3–30.

Gallagher, K., Brown, R. 1999. The Mesozoic denudation history of the Atlantic margins of southern Africa and southeast Brazil and the relationship to offshore sedimentation. Geological Society, London, Special Publications 153, 41–53.

Garçon, M., Chauvel, C., France-Lanord, C., Huyghe, P., Lavé, J. 2013. Continental sedimentary processes decouple Nd and Hf isotopes. Geochim. Cosmochim. Acta 121, 177–195.

Garçon, M., Chauvel, C. 2014. Where is basalt in river sediments, and why does it matter? Earth and Planetary Science Letters 407, 61-69.

Gingele, F. X., Müller, P. M., & Schneider, R. R. (1998). Orbital forcing of freshwater input in the Zaire Fan area—clay mineral evidence from the last 200 kyr. *Palaeogeography, Palaeoclimatology, Palaeoecology*, *138*(1-4), 17-26.

Godet, A., Bodin, S., Adatte, T., Föllmi, K.B. 2008. Platform-induced clay–mineral fractionation along a northern Tethyan basin–platform transect: implications for the interpretation of Early Cretaceous climate change (Late Hauterivian–Early Aptian). Cret. Res. 29, 830–847.

Goldstein, S.L., Hemming, S.R. 2003. Long lived isotopic tracers in oceanography, paleoceanography, and ice sheet dynamics. In: Elderfield, H., Turekian, K.K. 2003 (Eds.), Treatise on Geochemistry. Elsevier, New York, 453–489.

Gradstein, F.M., Ogg, J.G., Schmitz, M.D., Ogg, G.M. 2012. The Geologic Time Scale 2012. Elsevier.

Green, P.F., Duddy, I.R., Japsen, P., Bonow, J.M., Malan, J.A. 2017. Post-breakup burial and exhumation of the southern margin of Africa. Basin Research 29, 96-127.

Green, P.F., Japsen, P., Chamlers, J.A., Bonow, J.M., Duddy, I.R. 2018. Gondwana Research 53, 58- 81.

Haq, B.U. 2014. Cretaceous eustasy revisited. Global and Planetary Change 113, 44-58.

Harman, R., Gallagher, K., Brown, R., Raza, A., Bizzi, L. 1998. Accelerated denudation and tectonic/geomorphic reactivation of the cratons of northeastern Brazil during the Late Cretaceous. Journal of Geophysical Research 103, 27,091– 27,105.

Hay, W.W., Floegel, S. 2012. New thoughts about the Cretaceous climate and oceans. Earth Sci. Rev. 115, 262–272.

Hesse, R. 1988. Diagenesis# 13. Origin of chert: Diagenesis of biogenic siliceous sediments. *Geoscience Canada*, 15(3), 171-192.

Japsen, P., Bonow, J.M., Green, P.F., Cobbold, P. R., Chiossi, D., Lilletveit, R., Magnavita, L.P., Pedreira, A. 2012. Episodic burial and exhumation in NE Brazil after opening of the South Atlantic. GSA Bulletin 124, 800-816.

Jochum, K. P., Weis, U., Schwager, B., Stoll, B., Wilson, S. A., Haug, G. H., Andreae, M. O., Enzweiler, J. 2016. Reference values following ISO guidelines for frequently requested rock reference materials. Geostandards and Geoanalytical Research, 40 (3), 333-350.

Karpoff, A.M., Destrigneville, C., Stille, P. 2007. Clinoptilolite as a new proxy of enhanced biogenic silica productivity in lower Miocene carbonate sediments of the Bahamas platform : isotopic and thermodynamic evidence. Chem. Geol., 245, 285–304.

Knidiri, A., Daoudi, L., El Ouahabi, M., Rhouta, B., Rocha, F., Fagel, N. 2014. Palaeogeographic controls on palygorskite occurrence in Maastrichtian-Palaeogene sediments of the Western High Atlas and Meseta Basins (Morocco). Clay Minerals 49 (4), 595-608.

Loncke, L., Roest, W. R., Klingelhoefer, F., Basile, C., Graindorge, D., Heuret, A., Marcaillou, B., Museur, T., Fanget, A. S., Mercier de Lépina, M. 2020. Transform Marginal Plateaus. Earth-Science Reviews 203 (April): 102940.

Loparev, A., Rouby, D., Chardon, D., Dall'Asta, M., Sapin, F., Bajolet, F., et al. (2021). Superimposed rifting at the junction of the Central and Equatorial Atlantic: Formation of the passive margin of the Guiana Shield. *Tectonics, 40,* e2020TC006159.

Lugmair, G.W., Marti, K. 1977. Sm-Nd-Pu timepieces in the Angra dos Reis meteorite. Earth and Planetary Science Letters 35, 273–284.

Martin, E. E., MacLeod, K. G., Jiménez Berrocoso, A., Bourbon, E. 2012. Water Mass Circulation on Demerara Rise during the Late Cretaceous Based on Nd Isotopes. Earth and Planetary Science Letters 327-328 (April): 111-20.

März, C., Beckmann, B., Franke, C., Vogt, C., Wagner, T., Kasten, S. 2009. Geochemical environment of the Coniacian–Santonian western tropical Atlantic at Demerara Rise. Palaeogeography, Palaeoclimatology, Palaeoecology 273, 286-301.

McConnell, R.B. 1968. Planation Surfaces in Guyana. The Geographical Journal 134, 506–520.

McLennan, S.M. 1993. Weathering and Global Denudation. The Journal of Geology 101, 295–303.

Monteiro, H. S., Vasconcelos, P. M. P., Farley, K. A., Lopes, C. A. M. 2018. Age and Evolution of Diachronous Erosion Surfaces in the Amazon: Combining (U-Th)/He and Cosmogenic ^{3}He Records. Geochimica et Cosmochimica Acta 229 (May): 162-83.

Moore, D.M., Reynolds, R.C. 1989. X-ray diffraction and the identification and analysis of clay minerals. X-ray diffraction and the identification and analysis of clay minerals.

Morais Neto, J.M., Hegarty, K.A., Karner, G.D., Alkmim, F.F. 2009. Timing and mechanisms for the generation and modification of the anomalous topography of the Borborema Province, northeastern Brazil. Marine and Petroleum Geology 26, 1070-1086.

Mourlot, Y., Roddaz M., Dera, G., Calvès, G., Kim, J.-H., Chaboureau, A.-C., Mounic, S., Raisson, F. 2018. Geochemical Evidence for Large-Scale Drainage Reorganization in Northwest Africa During the Cretaceous. Geochemistry, Geophysics, Geosystems, 1690-1712.

Nederbragt, A.J., Thurow, J., Pearce, R. 2007. Sediment composition and cyclicity in the Mid-Cretaceous at Demerara Rise, ODP Leg 207. In: Mosher, D.C., Erbacher, J., Malone, M.J., et al. (Eds.), Proc. ODP Sci. Results 207, 1–31.

Nesbitt, H.W., Young, G.M. 1982. Early Proterozoic climates and plate motions inferred from major element chemistry of lutites. Nature 299, 715–717.

O'Brien, C.L., Robinson, S.A., Pancost, R.D., Sinninghe Damsté, J.S., Schouten, S., Lunt, D.J., Alsenz, H., Bornemann, A., Bottini, C., Brassell, S.C., Farnsworth, A., Forster, A., Huber, B.T., Inglis, G.N., Jenkyns, H.C., Linnert, C., Littler, K., Markwick, P., McAnena, A., Mutterlose, J., Naafs, B.D.A., Pütmann, W., Sluijs, A., van Helmond, N.A.G.M., Vellekoop, J., Wagner, T., Wrobel, N.K. 2017. Cretaceous sea-surface temperature evolution: Constraints from TEX86 and planktonic foraminiferal oxygen isotopes. Earth-Science Reviews 172, 224–247.

Petschick, R. 2001. MacDiff. Freeware scientific graphical analysis software for X-ray diffraction profiles. Frankfurt, Germany.

Peulvast, J.-P., Bétard, F. 2015. A History of Basin Inversion, Scarp Retreat and Shallow Denudation: The Araripe Basin as a Keystone for Understanding Long-Term Landscape Evolution in NE Brazil." Geomorphology, Patterns and rates of Cenozoic landscape change in orogenic and post-orogenic settings, 233 (March): 20-40.

Pierrehumbert, R.T. 2002. The hydrologic cycle in deep-time climate problems. Nature 419, 191-198.

Pletsch, T., Daudi, L., Chamley, H., Deconinck, J.F., Charroud, M. 1996. Palaeogeographic controls on palygorskite occurrence in mid-Cretaceous sediments of Morocco and adjacent basins. Clay Minerals 31, 403-416.

Potter, P. E. 1997. The Mesozoic and Cenozoic Paleodrainage of South America: A Natural History. Journal of South American Earth Sciences 10 (5): 331-44.

Raymo, M.E., Ruddiman, W.F., Froelich, P.N. 1988. Influence of late Cenozoic mountain building on ocean geochemical cycles. Geology 16, 649–653.

Riech, V., von Rad, U. 1979. Silica diagenesis in the Atlantic Ocean: diagenetic potential and transformations. *Deep drilling results in the Atlantic Ocean: Continental margins and paleoenvironment, 3*, 315-340.

Robert, C. 1981. Santonian to Eocene palaeogeographic evolution of the Rio Grande Rise (South Atlantic) deduced from clay-mineralogical data (DSDP legs 3 and 39). Palaeogeography, Palaeoclimatology, Palaeoecology 33, 311–325.

Roddaz, M., Viers, J., Brusset, S., Baby, P., Boucayrand, C., Hérail, G. 2006. Controls on weathering and provenance in the Amazonian foreland basin: Insights from major and trace element geochemistry of Neogene Amazonian sediments. Chem Geol, 226, 31–65

Roddaz, M., Dera, G., Mourlot, Y., Calvès, G., Kim, J.H., Chaboureau, A.-C., Mounic, S., Raisson, F. 2021. Provenance constraints on the Cretaceous-Paleocene erosional history of the Guiana Shield as determined from the geochemistry of clay-size fraction of sediments from the Arapaima-1 well (Guyana-Suriname basin). Marine Geology 434, 106233.

Ruffell, A., McKinley, J.M., Worden, R.H. 2002.Comparison of clay mineral stratigraphy to other proxy palaeoclimate indicators in the Mesozoic of NW Europe. Philosophical Transactions of the Royal Society London A 360, 675-693.

Sapin, F., Davaux, M., Dall'asta, M., Lahmi, M., Baudot, G., and Ringenbach, J.-C. 2016. Post-rift subsidence of the French Guiana hyper-oblique margin : from rift-inherited subsidence to Amazon deposition effect. Geological Society, London, Special Publications, 431 (1), 125–144.

Söderlund, U., Patchett, P.J., Vervoort, J.D., Isachsen, C.E. 2004. The 176Lu decay constant determined by Lu–Hf and U–Pb isotope systematics of Precambrian mafic intrusions. Earth and Planetary Science Letters 219, 311–324.

Stokke, E.W., Jones, M.T., Riber, L., Hflidason, H., Midtkandal, I., Schultz, B.P., Svensen, H.H. 2021. Rapid and sustained environmental responses to global warming: the Paleocene–Eocene Thermal Maximum in the eastern North Sea. Clim. Past 17, 1989–2013.

Taylor, S.R., McLennan, S.M. 1985. The Continental Crust: Its Composition and Evolution. An Examination of the Geochemical Record Preserved in Sedimentary Rocks. Blackwell Scientific Publications, Oxford, p. 312.

Théveniaut, H., Freyssinet, P. 2002. Timing of lateritization on the Guiana Shield: synthesis of paleomagnetic results from French Guiana and Suriname. Palaeogeography, Palaeoclimatology, Palaeoecology 178, 91-117.

Thiry, M. 2000. Palaeoclimatic interpretation of clay minerals in marine deposits: an outlook from the continental origin. Earth-Science Reviews 49, 201-221.

Vervoort, J.D., Patchett, P.J., Blichert-Toft, J., Albarède, F. 1999. Relationships between Lu–Hf and Sm–Nd isotopic systems in the global sedimentary system. Earth and Planetary Science Letters 168, 79–99.

Vervoort, J.D., Plank, T., Prytulak, J. 2011. The Hf–Nd isotopic composition of marine sediments. Geochim. Cosmochim. Acta 75, 5903–5926.

Wang, Y., Huang, C., Sun, B., Quan, C., Wu, J., Lin, Z. 2014. Paleo-CO_2 variation trends and the Cretaceous greenhouse climate. Earth-Science Reviews, 129, 136-147.

West, A.J., Galy, A., Bickle, M. 2005. Tectonic and climatic controls on silicate weathering. Earth and Planetary Science Letters 235, 211–228.

West, A. J. 2012. Thickness of the chemical weathering zone and implications for erosional and climatic drivers of weathering and for carbon-cycle feedbacks. Geology, 40 (9), 811-814.

Weis, D., Kieffer, B., Maerschalk, C., Pretorius, W., Barling, J. 2005. High-precision Pb-Sr-Nd-Hf isotopic characterization of USGS BHVO-1 and BHVO-2 reference materials. Geochemistry, Geophysics, Geosystems 6.

Weis, D., Kieffer, B., Maerschalk, C., Barling, J., Jong, J. de, Williams, G.A., Hanano, D., Pretorius, W., Mattielli, N., Scoates, J.S., Goolaerts, A., Friedman, R.M., Mahoney, J.B. 2006. High-precision isotopic characterization of USGS reference materials by TIMS and MC-ICP-MS. Geochemistry, Geophysics, Geosystems 7.

White, A.F., Blum, A.E. 1995. Effects of climate on chemical weathering in watersheds. Geochimica et Cosmochimica Acta 59 (9), 1729-1747.

Yang, W., Escalona, A. 2011. "Tectonostratigraphic Evolution of the Guyana Basin." AAPG Bulletin 95 (8): 1339-68.

Young, GM M., Nesbitt, H., W. 1999. Paleoclimatology and provenance of the glaciogenic Gowganda Formation (Paleoproterozoic), Ontario, Canada: A chemostratigraphic approach. GSA Bulletin 111 (2), 264-274.

Zhao, W., Sun, Y., Balsam, W., Lu, H., Liu, L., Chen, J., & Ji, J. (2014). Hf-Nd isotopic variability in mineral dust from Chinese and Mongolian deserts: implications for sources and dispersal. *Scientific Reports*, *4*(1), 1-6.

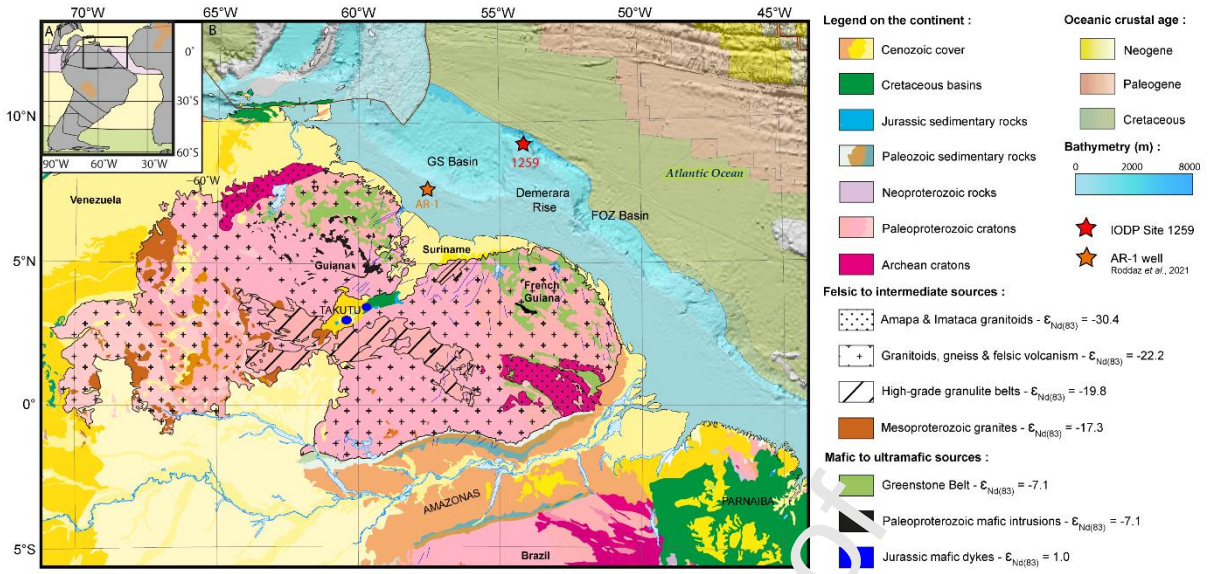

Figure 1 – A. Palaeogeographic map of the South American continent for the Campanian (83 Ma ; www.odsn.de) with the humid climatic belt in pink, the arid climatic belt in yellow, the mid-latitude warm humid belt in green and the evaporitic belts in orange (according to Hay & Floegel, 2012). B. Geological map of the northeastern Brazilian margin with the main $\varepsilon_{Nd(t)}$ units of the Guiana Shield from Roddaz *et al.* (2021) calculated at 83 Ma and location of Site 1259 and AR-1well from Roddaz et al., 2021.

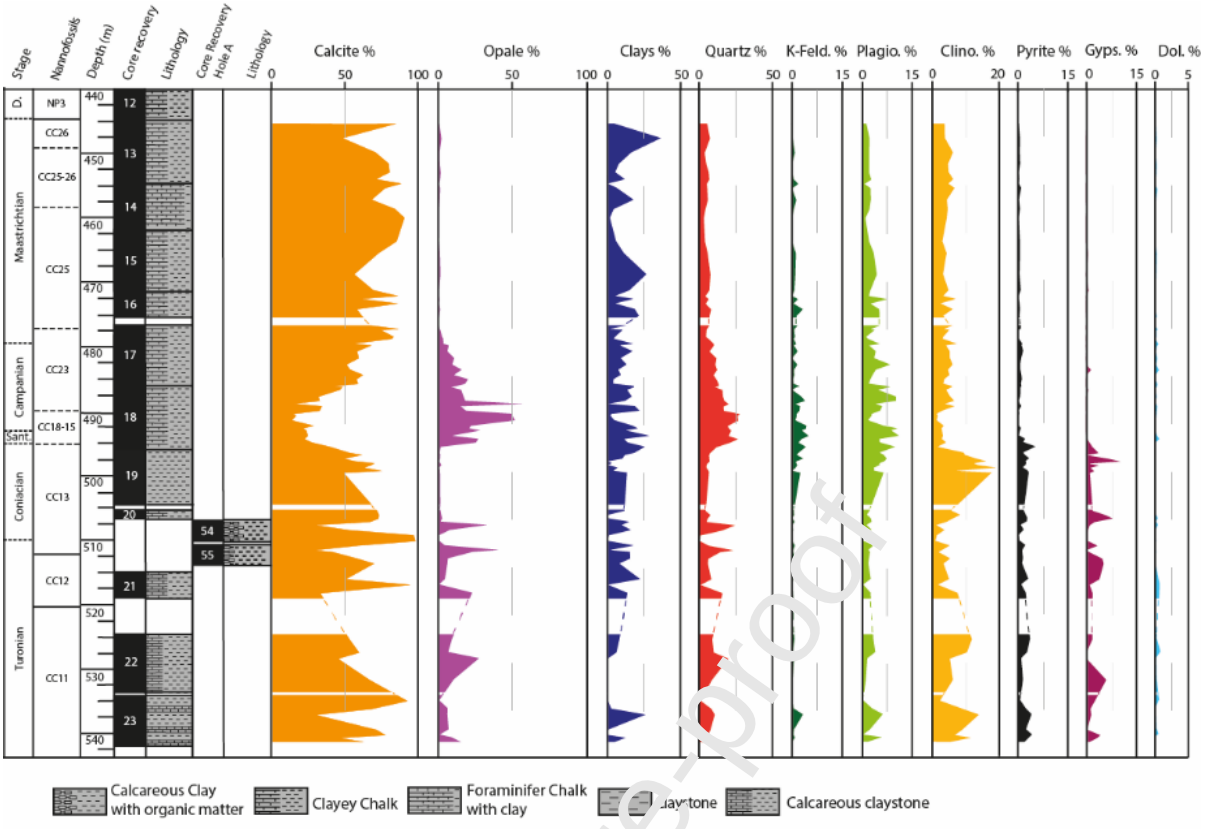

Figure 2 – Lithology, biostratigraphy and mineralogy at Site 1259. Abbreviations : Sant. = Santonian, D. = Danian.

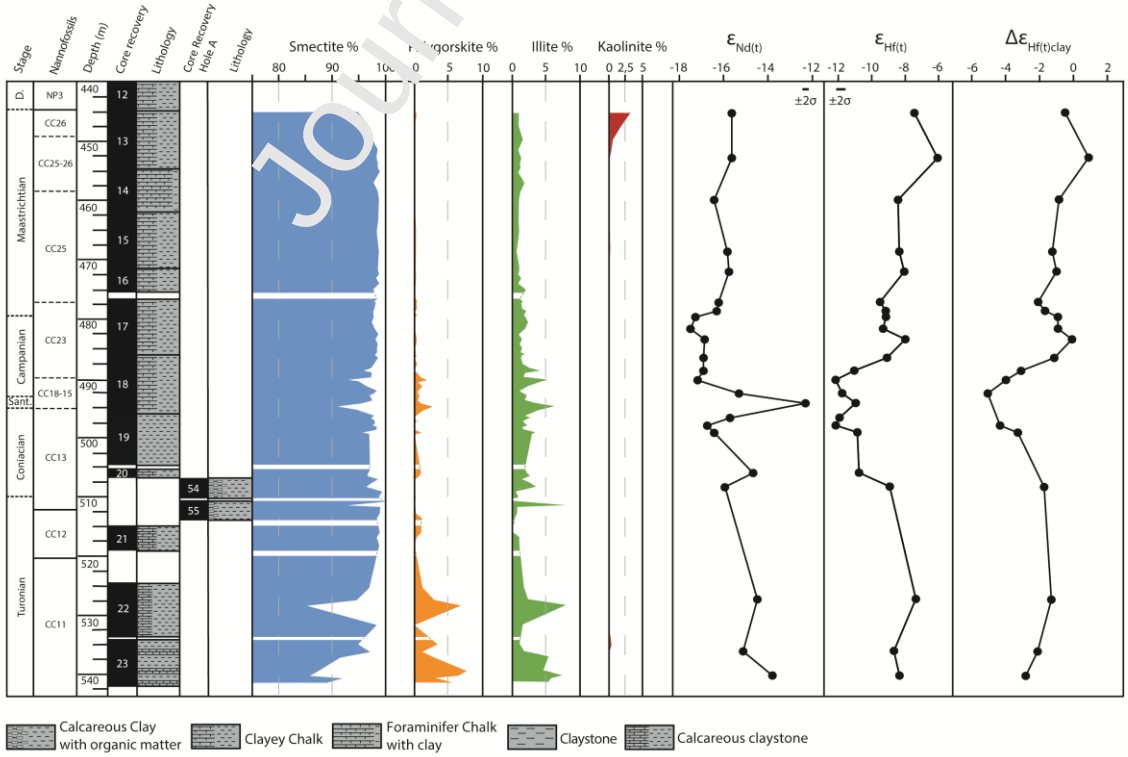

Figure 3 – Lithology, biostratigraphy, clay mineralogy, $\varepsilon_{Nd(t)}$, $\varepsilon_{Hf(t)}$ and $\Delta\varepsilon_{Hf(t)clay}$ of ODP Site 1259. Abbreviations : Sant. = Santonian, D. =Danian. The black bars corresponds to the external reproductibility (2 s.d) of ε_{Nd} and ε_{Hf} based on repeated analyses of JMC 475 and JNDi standards.

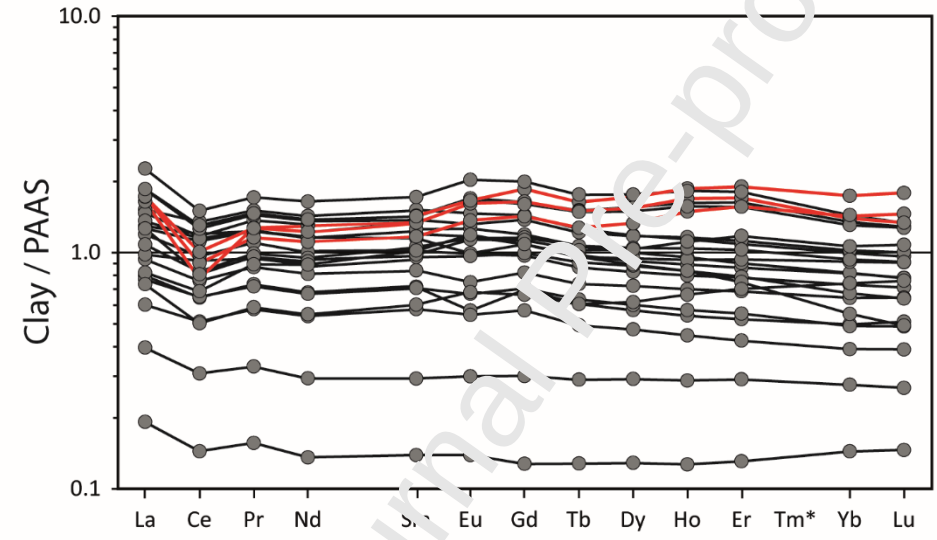

Figure 4 – Shale-normalized (PAAS ; Taylor and McLennan, 1985) REE patterns for the clay fraction of Site 1259. The three samples in red presents a slight negative Ce anomaly and a slight enrichment in HREE.

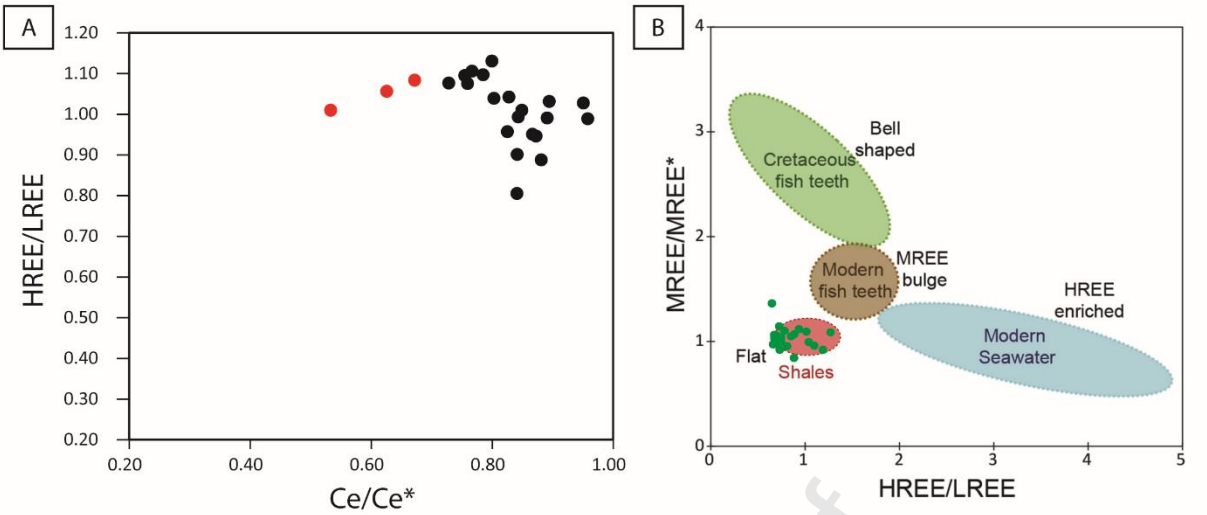

Figure 5 – A. HREE/LREE vs Ce/Ce* diagram with the three samples in red presenting the most negative cerium anomaly. B. MREE/MREE* vs HREE/LREE diagram. The data of this study appears in green dots and were potted on the diagram of Roddaz et al., 2021. The samples plotted in the "flat" REE patterns end member characteristic of continental clays.

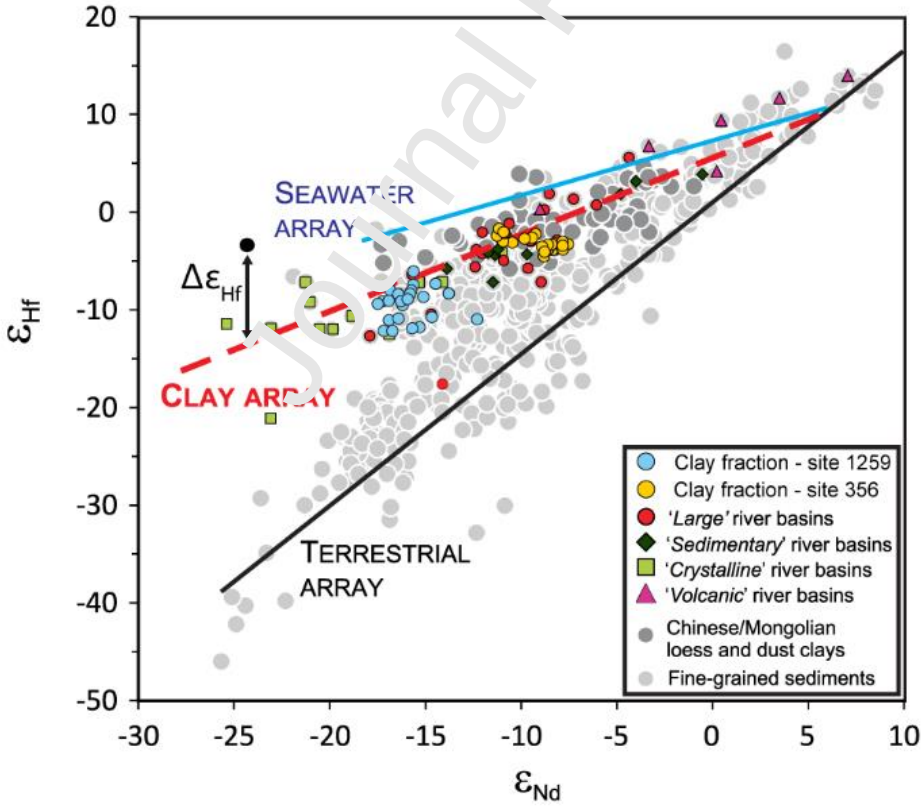

Figure 6 – Nd and Hf isotopic composition of clay-size fractions at Site 1259 and Site 356 (Corentin et al., 2022) together with data for modern river clays (modified from Bayon *et al*, 2016). The Clay Array corresponds to the correlation displayed by ε_{Nd} and ε_{Hf} in modern clay-size fractions (Bayon *et al.*, 2016). $\Delta\varepsilon_{Hf}$ corresponds to the vertical ε_{Hf} deviation of any sample relative to the clay array, which reflects the intensity of chemical weathering.

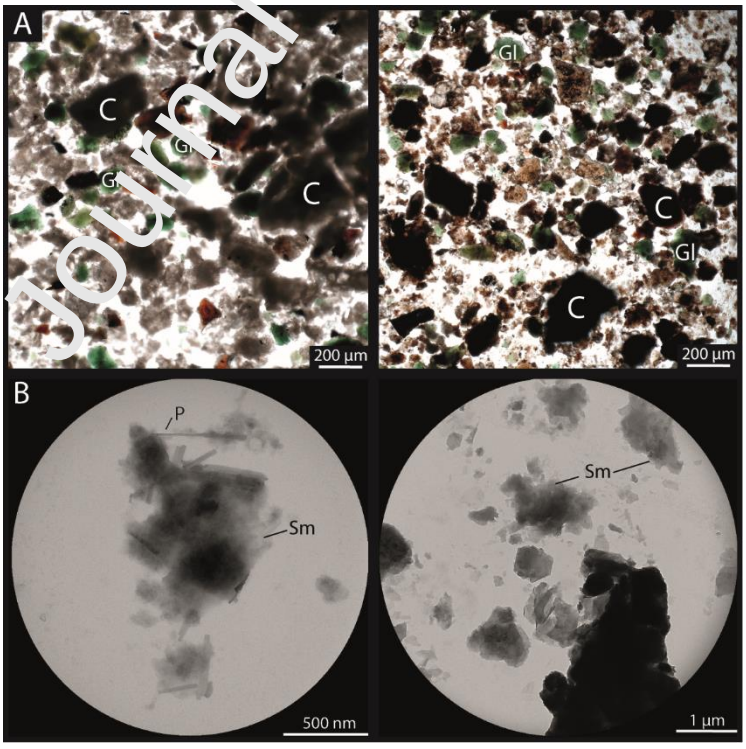

Figure 7 – A – Smear slides of the samples 18r7w31 (left) and 18rCCw3 (right) containing clay minerals (dark brown) noted “C” and glauconite aggregate (green) noted “Gl”. B – Transmission electron micrographs (TEM) of detrital particles of smectite with flake shape (left, sample 22r3w100) and short fibres of detrital palygorskite with smectite particles (right, sample 18r7w80).

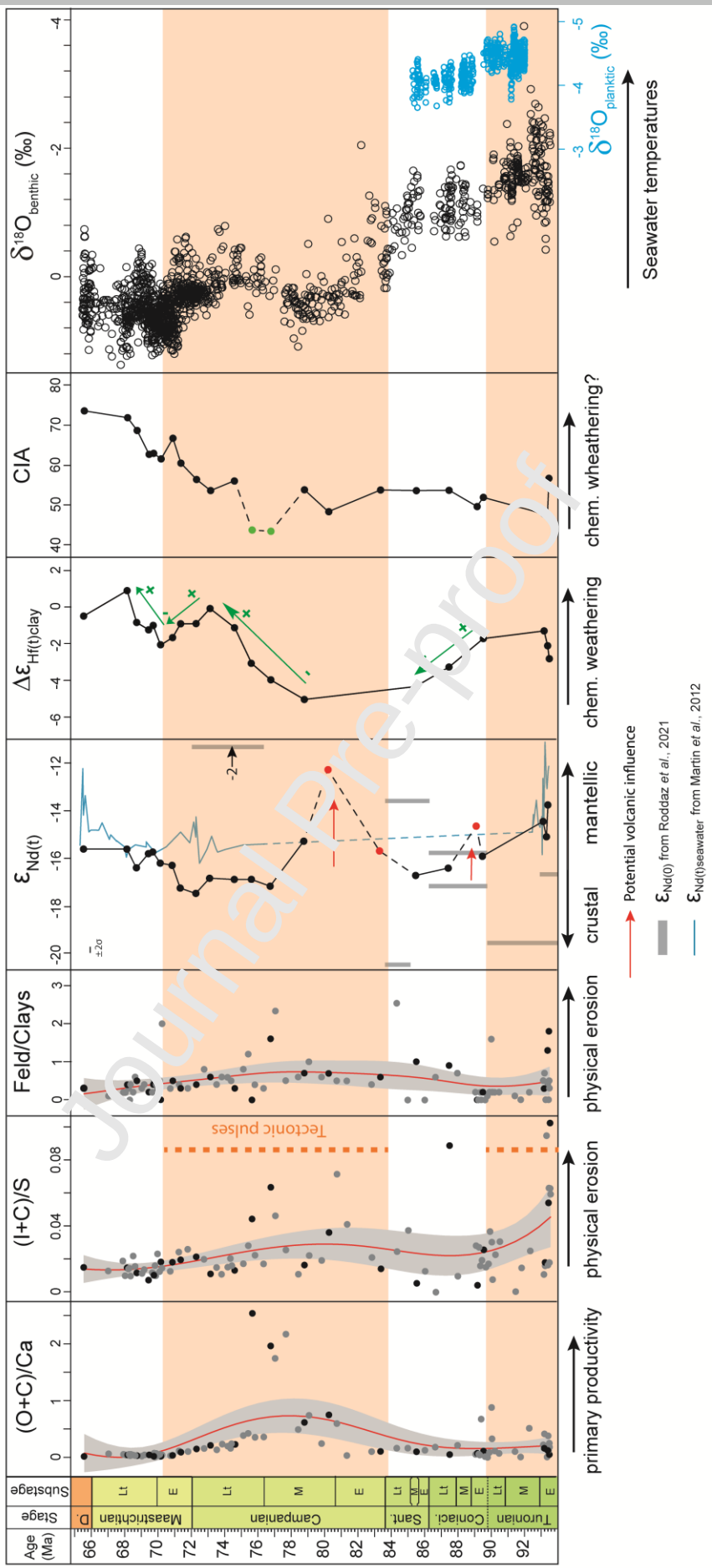

Figure 8 –Evolution of the (Opal+Clinoptilolite)/Calcite ((O+C)/Ca),

(Illite+Chlorite)/Smectite ((I+C)/S), Feldspar/clays (Feld/Clays), $\varepsilon_{Nd(t)}$, $\Delta\varepsilon_{Hf(t)clay}$ and CIA for Site 1259 clay-size fractions during the Upper Cretaceous. The global $\delta^{18}O_{benthic}$ (Friedrich *et al.*, 2012) and local $\delta^{18}O_{planktic}$ signals (Bornemann *et al.*, 2008) are shown for comparison. The grey and black dots correspond respectively to samples analysed by XRD only and for which both geochemical and mineralogical analyses were conducted. The white and blue dots correspond to literature data. Finally, the red and green dots are considered as anomalous values (see text for discussion). The black bar corresponds to the external reproductibility (2 s.d) of ε_{Nd} on repeated analyses of JNDi standard. Smoothed curves with their 95% confidence interval have been calculated using Kernel regressions for (O+C)/Ca, (I+C)/S and Feld/Clays ratios, with a bandwidth of 5 m.y. representing maximal time resolution. The Nd isotopic compositon of Roddaz et al., 2021 appears in grey rectangle and the Nd isotopic composition of Martin et al., 2012 appears in blue. The green arrows highlighted the evolution of chemical weathering on the margin. Abbreviations : Coniac. = Coniacian, Sant. = Santonian, D. = Danian, E = Early, M = Middle, Lt = Late, chem. = chemical.

Sample	13r1w57-60	13r6w67-70	14r4w110-113	15r5w77-80	16r1w55-57	17r1w69-72	17r2w69-72	17r3w22-24
Age	65.57	68.17	68.75	69.46	69.73	70.18	70.89	71.38
wt%								
Al_2O_3	3.61	3.77	2.21	5.19	2.83	2.65	2.51	3.14
Na_2O	0.36	0.41	0.28	0.78	0.44	0.44	0.34	0.54
K_2O	0.11	0.10	0.07	0.47	0.19	0.20	0.13	0.26
TiO_2	0.14	0.14	0.09	0.21	0.12	0.11	0.11	0.15
SiO_2	13.04	15.32	9.29	19.45	11.63	11.51	11.77	16.46
Fe_2O_3	1.36	1.27	0.87	1.82	1.23	0.98	0.82	0.85
MnO	0.08	0.06	0.05	0.05	0.04	0.03	0.03	0.01
MgO	0.59	0.66	0.47	0.89	0.54	0.53	0.52	0.58
CaO	42.84	40.59	46.40	35.56	43.59	43.42	43.50	35.76
P_2O_5	0.06	0.05	0.03	0.08	0.06	0.06	0.04	0.04
Cr_2O_3	0.00	0.00	0.00	0.01	0.00	0.00	0.00	0.00
LOI	36.90	37.31	39.10	35.17	37.54	37.62	38.17	33.63
ppm								
La	49.41	48.41	45.61	58.15	56.18	5[illegible]02	35.81	30.53
Ce	95.62	88.93	76.96	107.49	93.32	91.3[illegible]	60.46	51.34
Pr	10.89	10.86	9.71	13.32	12.10	[illegible]	7.66	6.49
Nd	39.22	39.56	34.03	48.40	44.55	39.01	27.57	23.00
Sm	6.65	6.97	5.65	8.42	7.66	[illegible]	4.67	3.97
Eu	1.27	1.36	1.07	1.58	1.43	1.07	0.81	0.61
Gd	5.05	5.56	4.52	6.71	6.42	[illegible]	3.83	3.25
Tb	0.75	0.83	0.67	0.97	0.94	0.74	0.57	0.47
Dy	4.31	4.68	3.88	5.53	5.[illegible]	4.42	3.38	2.67
Ho	0.88	0.95	0.79	1.13	1.15	0.93	0.69	0.54
Er	2.46	2.57	2.23	3.10	3.[illegible]	2.67	1.95	1.49
Tm	0.99	0.99	0.93	1.07	1.08	1.21	0.91	0.83
Yb	2.30	2.31	2.06	2.81	2.[illegible]	2.58	1.81	1.40
Lu	0.34	0.34	0.31	0.42	0.43	0.39	0.28	0.22
Hf	3.16	3.02	3.21	3.[illegible]	3.44	3.90	3.02	2.68
Zr	123.00	118.00	135.00	[illegible]	142.00	157.00	124.00	107.00

Sample	17r4w70-73	17r5w99-100,5	18r1w71-73	18r2w148-150	18r3w148-150	18r5w70-72	18r7w30,5-32	19r1w123-125
Age	72.31	73.15	74.62	[illegible]65	76.77	78.79	80.25	83.36
wt%								
Al_2O_3	4.45	3.98	5.79	4.38	3.49	8.11	6.01	3.35
Na_2O	0.89	0.88	1.1[illegible]	1.43	1.17	1.63	1.42	0.79
K_2O	0.46	0.52	0.[illegible]8	0.88	0.65	1.48	1.62	0.26
TiO_2	0.18	0.17	[illegible]23	0.18	0.14	0.33	0.23	0.14
SiO_2	24.41	24.64	31.[illegible]3	59.93	54.01	45.93	47.63	12.73
Fe_2O_3	1.22	1.04	[illegible]9	0.93	0.85	2.31	4.30	1.49
MnO	0.01	0.01	0.02	0.01	0.01	0.01	0.01	0.02
MgO	0.76	0.[illegible]4	1.01	0.71	0.63	1.46	1.42	0.69
CaO	33.12	31.26	28.00	12.37	12.78	14.15	15.72	33.92
P_2O_5	0.05	0.05	0.09	0.08	0.04	0.24	1.59	0.56
Cr_2O_3	0.01	0.00	0.01	0.01	0.01	0.01	0.03	-
LOI	31.95	33.62	30.26	19.58	26.50	24.68	18.83	39.66
ppm								
La	29.39	22.99	37.53	15.14	7.33	41.28	62.81	65.83
Ce	51.73	40.62	73.51	24.53	11.48	66.24	61.87	71.79
Pr	6.36	5.08	8.35	2.91	1.38	8.75	11.23	10.23
Nd	22.68	18.25	30.15	9.95	4.61	32.21	43.93	37.67
Sm	3.93	3.20	5.32	1.63	0.77	5.87	7.95	6.48
Eu	0.72	0.59	1.04	0.32	0.15	1.24	1.79	1.48
Gd	3.29	2.66	4.64	1.40	0.60	5.40	8.66	6.64
Tb	0.49	0.38	0.70	0.22	0.10	0.83	1.27	0.99
Dy	2.81	2.21	4.12	1.36	0.60	4.90	8.05	6.22
Ho	0.57	0.44	0.83	0.29	0.13	1.03	1.85	1.48
Er	1.57	1.21	2.25	0.83	0.37	2.93	5.42	4.46
Tm	0.83	0.78	0.93	0.75	0.74	1.05	1.39	1.26
Yb	1.38	1.10	1.90	0.78	0.41	2.64	4.90	4.02
Lu	0.21	0.17	0.28	0.12	0.06	0.39	0.77	0.63

Hf	2.45	1.99	2.47	1.18	1.14	2.79	2.13	1.94
Zr	92.00	76.00	95.00	47.00	42.00	107.00	84.00	61.00

Sample	19r2w102-104	19r3w70,5-72	20r1w94-96	54r2w32-34,5	21r2w60-63	22r3w3-5	23r2w64-66	23r5w23-25
Age	85.51	87.48	89.15	89.52	91.77	93.17	93.38	93.47
wt%								
Al_2O_3	4.48	4.41	3.57	3.76	0.48	3.97	4.18	1.67
Na_2O	1.05	1.02	1.01	0.98	0.03	1.15	1.27	0.36
K_2O	0.36	0.39	0.28	0.25	0.01	0.50	0.45	0.07
TiO_2	0.18	0.17	0.16	0.14	0.02	0.16	0.17	0.08
SiO_2	16.99	16.34	16.36	17.46	1.70	19.63	21.13	6.99
Fe_2O_3	1.44	1.26	1.30	1.28	0.16	1.26	1.29	1.11
MnO	0.02	0.02	0.02	0.02	0.02	0.01	0.01	0.03
MgO	0.81	0.83	0.70	0.79	0.64	0.90	0.80	0.58
CaO	29.04	25.56	27.16	25.39	52.91	22.90	26.01	39.02
P_2O_5	1.08	1.03	0.77	0.23	0.06	0.75	1.39	1.03
Cr_2O_3	-	-	-	-	-	0.03	0.03	-
LOI	39.20	43.74	41.96	41.97	43.68	43.19	38.18	42.75
ppm La								
	70.60	48.36	66.07	31.43	-	2[illegible]06	70.98	86.56
Ce	100.44	64.54	80.17	54.59	-	[illegible]9.93	103.86	119.53
Pr	12.74	8.49	11.20	7.88	-	[illegible].18	12.94	15.12
Nd	46.31	31.06	41.57	30.13	-	18.58	46.83	55.74
Sm	7.94	5.45	7.42	5.66	-	3.34	7.90	9.54
Eu	1.83	1.23	1.74	1.28	-	0.73	1.79	2.20
Gd	7.62	5.27	7.66	5.05	-	3.09	7.47	9.30
Tb	1.17	0.79	1.16	0.74	-	0.47	1.15	1.36
Dy	7.28	4.84	7.22	4.17	-	2.89	6.99	8.25
Ho	1.61	1.10	1.68	0.83	-	0.66	1.56	1.81
Er	4.65	3.35	4.86	2.14	-	2.00	4.45	5.15
Tm	1.25	1.11	1.31	[illegible]0	-	0.91	1.28	1.34
Yb	3.80	3.00	3.93	1.5[illegible]	-	2.09	3.69	4.06
Lu	0.56	0.47	0.58	[illegible].21	-	0.33	0.55	0.58
Hf	2.11	1.94	1.86	1.44	-	1.91	2.21	2.10
Zr	76.00	72.00	70.00	[illegible].00	-	74.00	81.00	75.00

Table 1 - Major elements concentrations measured by XRF in the bulk sediment and rare earth element concentrations measured by ICP-MS in the clay fraction in the samples of Site 1259.

Sample	Age	$^{143}Nd/^{144}Nd$	Error	$\varepsilon_{Nd(0)}$	2 σ	$\varepsilon_{Nd(t)}$		$\varepsilon_{Hf(0)}$	2 σ	$\varepsilon_{Hf(t)}$	$\Delta\varepsilon_{Hf}$
		$^{176}Hf/^{177}Hf$	Error								
13r1w57-60	65.57	0.511789	0.000005	-16.41	0.09	-15.63	0.282552	0.000005	-8.25	0.16	-7.45	-0.49
13r6w67-70	68.17	0.511789	0.000004	-16.41	0.08	-15.63	0.282591	0.000006	-6.86	0.20	-6.07	0.90
14r4w110-113	68.75	0.511745	0.000005	-17.26	0.10	-16.42	0.282521	0.000006	-9.33	0.21	-8.43	-0.85
15r5w77-80	69.46	0.511778	0.000006	-16.63	0.12	-15.83	0.282527	0.000006	-9.12	0.20	-8.36	-1.24
16r1w55-57	69.73	0.511780	0.000006	-16.57	0.12	-15.76	0.282537	0.000007	-8.77	0.23	-8.06	-1.00
17r1w69-72	70.18	0.511754	0.000007	-17.08	0.13	-16.22	0.282491	0.000006	-10.39	0.22	-9.50	-2.08
17r2w69-72	70.89	0.511751	0.000005	-17.16	0.09	-16.31	0.282499	0.000005	-10.12	0.18	-9.17	-1.67
17r3w22-24	71.38	0.511702	0.000006	-18.09	0.11	-17.26	0.282497	0.000004	-10.18	0.15	-9.15	-0.92
17r4w70-73	72.31	0.511690	0.000006	-18.33	0.11	-17.49	0.282493	0.000006	-10.34	0.21	-9.32	-0.91
17r5w99-100,5	73.15	0.511723	0.000005	-17.69	0.10	-16.85	0.282529	0.000003	-9.04	0.11	-8.00	-0.08
18r1w71-73	74.62	0.511720	0.000007	-17.75	0.13	-16.91	0.28250[illegible]	[illegible]000005	-9.96	0.17	-9.09	-1.13
18r2w148-150	75.65	0.511716	0.000005	-17.84	0.09	-16.91	0.28[illegible]	0.000007	-12.02	0.23	-11.04	-3.09
18r3w148-150	76.77	0.511702	0.000011	-18.11	0.21	-17.19	0.28[illegible]	0.000008	-13.45	0.28	-12.15	-3.98
18r5w70-72	78.79	0.511801	0.000005	-16.17	0.10	-15.31	0.282433	0.000007	-12.46	0.24	-11.76	-5.05
18r7w30,5-32	80.25	0.511954	0.000004	-13.20	0.09	-12.31	0.282503	0.000006	-9.99	0.21	-10.95	-6.58
19r1w123-125	83.36	0.511775	0.000004	-16.68	0.09	-15.71	0.282468	0.000006	-11.22	0.22	-11.92	-4.90
19r2w102-104	85.51	0.511721	0.000005	-17.74	0.10	-16.74	0.282448	0.000009	-11.92	0.32	-12.15	-4.32
19r3w70,5-72	87.48	0.511737	0.000005	-17.42	0.09	-16.42	0.282479	0.000008	-10.82	0.27	-10.86	-3.28
20r1w94-96	89.15	0.511827	0.000006	-15.67	0.13	-14.67	0.282499	0.000004	-10.11	0.16	-10.76	-4.54
54r2w32-34,5	89.52	0.511765	0.000008	-16.8[illegible]	0.16	-15.94	0.282512	0.000008	-9.67	0.29	-8.93	-1.73
22r3w3-5	93.17	0.511835	0.000004	-15.[illegible]	0.08	-14.48	0.282561	0.000005	-7.92	0.18	-7.37	-1.30
23r2w64-66	93.38	0.511798	0.000005	-16.23	0.10	-15.12	0.282543	0.000007	-8.55	0.24	-8.68	-2.12
23r5w23-25	93.47	0.511866	0.000007	-14.90	0.13	-13.80	0.282559	0.000006	-8.00	0.21	-8.35	-2.81

Table 2 – Nd-Hf isotopic ratios and compositions measured by MC-ICP-MS in the samples of Site 1259.

Declaration of interests

☐The authors declare that they have no known competing financial interests or personal relationships that could have appeared to influence the work reported in this paper.

☒The authors declare the following financial interests/personal relationships which may be considered as potential competing interests:

Pauline Corentin reports financial support was provided by International Ocean Discovery Program.

Highlights

Use of paired Hf-Nd isotopes to constrain continental weathering in deep-time.

Enhanced silicate weathering concomitant with an uplift phase of the Guiana craton.
Tectonic uplift contributed to the late Cretacous cooling.
During relative tectonic quiescence, climate seems to control the evolution of chemical weathering intensity.

Accelerating chemical weathering acted as an additional factor stabilizing colder climate conditions.